

Texture- and Stress-Dependent Electromechanical Response in Ferroelectric PZT: Insights from a Micromechanical Model

Saujatya Mandal¹, Debashish Das^{1*}

Department of Mechanical Engineering, Indian Institute of Science, Bengaluru, India

Abstract

The performance of $\text{PbZr}_{0.52}\text{Ti}_{0.48}\text{O}_3$ (PZT)-based microelectromechanical systems (MEMS) and other piezoelectric devices can be significantly enhanced by optimizing crystallographic texture, which directly influences polarization switching and electromechanical response. However, the combined effect of texture and residual stress on the nonlinear behavior of PZT remains poorly understood, particularly in morphotropic-phase-boundary (MPB) compositions, where both tetragonal and rhombohedral domain switching mechanisms coexist. While several computational models have been developed to predict the response of ferroelectric materials, most studies either focus exclusively on tetragonal ceramics, require computationally expensive self-consistent schemes, or fail to explicitly capture key experimental observables, such as butterfly loops and D_3 - E_3 hysteresis loops. Furthermore, the lack of accessible numerical implementations limits the ability of experimentalists to engage with and refine these models. To address these challenges, this work presents an efficient micro-electromechanical model based on Hwang et al. (1998), implemented in an open-source MATLAB framework to predict the effects of preferred crystallographic orientation and residual stress on polarization switching in MPB PZT. Despite its simplicity, the model successfully captures key experimentally observed trends, making it an invaluable tool for understanding domain-switching processes in ferroelectrics. By making the code freely available, this study provides a practical and scalable computational approach that allows researchers—especially experimentalists—to simulate, analyze, and refine polarization switching behavior, bridging the gap between theoretical modeling and real-world ferroelectric device optimization.

Keywords: Morphotropic phase boundary (MPB) PZT, Crystallographic texture and residual stress, Ferroelectric domain switching, Electromechanical response modeling, Open-source MATLAB code

* Corresponding Author: ddas@iisc.ac.in

1. Introduction

Ferroelectric materials, particularly lead zirconate titanate ($\text{PbZr}_{0.52}\text{Ti}_{0.48}\text{O}_3$, PZT), are extensively used in sensors, actuators, energy harvesting systems, RF switches, inkjet printer heads, biosensors, ultra-low power mechanical logic, millimeter-scale robotics, and Micro-Electromechanical Systems (MEMS) due to their exceptional piezoelectric properties¹⁻⁶. These remarkable electromechanical properties originate from PZT's perovskite crystal structure and its morphotropic phase boundary (MPB), where rhombohedral and tetragonal phases coexist⁷. The MPB is particularly important as it enhances domain mobility and electromechanical coupling by providing multiple energetically equivalent polarization states⁷. However, the overall performance of PZT is highly dependent on crystallographic texture and residual stress, both of which significantly influence polarization switching, domain wall motion, ferroelasticity, and the overall piezoelectric response⁸⁻¹².

Enhancing grain orientation (texturing) in polycrystalline PZT has proven to be an effective strategy for improving electromechanical properties, bridging the performance gap between bulk ceramics and single crystals while retaining the advantages of ceramic processing^{8,13-15}. Various texturing techniques, such as magnetic field alignment, hot press sintering, templated grain growth, and seeded tape casting, have enabled the fabrication of highly textured bulk PZT ceramics with enhanced properties¹⁶⁻¹⁸. Notably, Li *et al.*⁸ reported the development of a “seed-passivated” tape-casting method to fabricate bulk $\langle 001 \rangle$ -textured PZT ceramics with $\sim 94\%$ aligned grains, achieving a Curie temperature of $\sim 360^\circ\text{C}$ and a piezoelectric coefficient (d_{33}) of ~ 760 pC/N—nearly double that of conventional PZT ceramics. Similarly, Lee *et al.*¹³ achieved a Lotgering orientation factor of $\sim 95\%$ in PZT-based ceramics using BaTiO_3 platelets, resulting in a 60% increase in field-induced strain compared to untextured samples. These advancements underscore the importance of controlling texture to enhance polarization rotation and domain switching, key factors in maximizing piezoelectric response. In thin-film PZT, where orientation and stress play an even more significant role, various chemical and physical deposition techniques have been developed^{19,20}, including chemical solution deposition (and sol-gel processing), RF magnetron sputtering, metal-organic chemical vapor deposition (MOCVD), and pulsed laser deposition (PLD). For instance, Yeo and Trolier-McKinstry²¹ demonstrated that highly (001)-oriented PZT thin films deposited on Ni foils exhibit a remanent polarization (P_r) of ~ 36 $\mu\text{C}/\text{cm}^2$ and a transverse

piezoelectric coefficient $|e_{31,f}| \approx 10.6 \text{ C/m}^2$ —significantly outperforming randomly oriented films. More recently, Das *et al.*¹⁰ demonstrated that a fully (001)-textured PZT thin film exhibits an effective piezoelectric coefficient ($d_{31,f}$) nearly 2.5 times larger than that of a (111)-textured film, a trend that aligns with findings by Du *et al.*²², who reported a similar 2.5-fold increase in d_{33} for (001)-oriented films.

While most studies report improved ferroelectric response for (001)/(100) textures, some studies have also reported improved response for $\{111\}$ ²³, $\{110\}$ ²⁴, or even randomly oriented PZT²⁵ near the MPB, which prevents unequivocal conclusions. These discrepancies in reported texture-dependent piezoelectric properties are further complicated by residual stress effects, which are often overlooked. Thin-film PZT is particularly susceptible to biaxial tensile residual stresses, especially when deposited on platinized silicon substrates, where substrate clamping effects restrict domain mobility and reduce field-induced strain^{12,26}. Furthermore, residual stresses can be different for films deposited with different crystallite orientation (or texture)²⁷, which can also lead to differences in reported properties^{11,28}. To fully understand the role of texture, it is therefore imperative to decouple the effects of crystallographic orientation and residual stress, an area where computational modeling provides valuable insights.

Most computational studies on ferroelectric domain switching have primarily focused on tetragonal ferroelectric ceramics, largely due to their simpler switching behavior²⁹⁻³¹. In contrast, significantly fewer studies have explored rhombohedral ferroelectrics^{32,33}, where the larger number of polarization variants introduces greater complexity in domain interactions and switching dynamics. Moreover, there are very few theoretical works that explicitly address the domain switching process in morphotropic ferroelectric ceramics, where both tetragonal and rhombohedral phases coexist^{34,35}. Even more scarce are studies explicitly addressing the effects of texture and residual stress on domain switching and electromechanical response in PZT at MPB. Among the limited efforts in this direction, Huber and Fleck's self-consistent crystal plasticity model³⁶ demonstrated that the electric field required for domain switching strongly depends on its angle relative to the polarization axis, predicting significant anisotropy in switching behavior. García *et al.*³⁷ developed a virtual Piezoresponse Force Microscopy (PFM) framework, integrating Electron Backscatter Diffraction (EBSD) with Finite Element Modeling (FEM) to show that grain orientation, residual stress, and epitaxial strain introduce local variations in switching behavior.

Their simulations revealed that (001)-textured grains exhibit enhanced polarization and switchability under compressive epitaxial strain, while (111)-oriented grains in randomly textured films demonstrate stronger responses due to stress-induced polarization rotation and asymmetric hysteresis loops. Murdoch and García³⁸ extended this work, employing Monte Carlo simulations and FEM to assess the relationship between texture strength and coercive field variations, showing that a strong (001) texture lowers coercive fields and enhances switching reliability. However, despite these advancements, existing models have several limitations. Most computational studies focus on single-phase tetragonal PZT, neglecting the complexities of MPB compositions, where both tetragonal and rhombohedral phases coexist. Fully self-consistent micromechanical models remain computationally expensive, making them impractical for large-scale simulations. Key experimental observables, such as butterfly loops and D_3 - E_3 hysteresis loops, are not explicitly captured, limiting direct comparisons with experimental measurements.

To address these limitations, this study employs a simplified micro-electro-mechanical model based on Hwang *et al.*²⁹, which, despite its simplicity, can capture key experimentally observed trends in texture- and stress-dependent switching behavior. While not as computationally intensive as self-consistent models or FEM, it provides a quantitative link between texture, residual stress, and polarization switching, making it highly practical for engineering applications. Furthermore, we open-source the code, allowing experimentalists and theorists alike to use, modify, and expand upon the framework, facilitating further model improvements and experimental validation. By bridging the gap between computational efficiency and experimental relevance, this work contributes to the development of scalable, experimentally verifiable models for MPB PZT.

2. Theoretical Model

Ferroelectric ceramics near the MPB exhibit complex electromechanical behavior due to the coexistence of tetragonal and rhombohedral phases. Prior models, including those by Hwang *et al.*^{29,39}, primarily considered tetragonal domain switching. However, near the MPB, an equal fraction of tetragonal and rhombohedral crystallites coexists, necessitating the incorporation of both domain switching and interphase transformations. This section presents an extended micro-electro-mechanical model that accounts for both tetragonal and rhombohedral switching

mechanisms and interphase transformations, explicitly incorporating polycrystalline matrix constraints.

2.1. Constitutive Laws for Crystallites

Each crystallite, whether tetragonal or rhombohedral, obeys the following two constitutive laws for the electric displacement vector D_i , and the strain tensor, ε_{ij} :

$$D_i = \kappa_{ij}E_j + d_{ikl}\sigma_{kl} + P_i^s \quad (1a)$$

$$\varepsilon_{ij} = d_{kij}E_k + s_{ijlm}\sigma_{lm} + \varepsilon_{ij}^s \quad (1b)$$

where κ , d , s and σ are dielectric permittivity, piezoelectric strain coefficient, elastic compliance, and stress tensors, respectively. E , P^s , ε^s are the electric field vector, spontaneous polarization vector, and spontaneous strain tensor, respectively.

2.2. Crystallographic Structures

- Tetragonal Phase:

The c axis of each tetragonal unit cell is parallel to the spontaneous polarization direction. The principal values of the spontaneous strain of each crystallite, in the local coordinate system, are:

$$\varepsilon_3^s = \frac{c - a_0}{a_0}; \quad \varepsilon_1^s = \varepsilon_2^s = \frac{a - a_0}{a_0} \quad (2)$$

where a and c are the lattice parameters of the tetragonal unit cell and a_0 is the lattice parameter of the cubic unit cell above the Curie temperature. We will, however, assume that $\varepsilon_1^s = \varepsilon_2^s = -\varepsilon_3^s/2$ with $\varepsilon_3^s = \varepsilon_0^T$ so that the tetragonal unit cell has the same volume as the cubic cell. The principal directions of the spontaneous strain in tetragonal unit cells are the c axis (ε_{33}) in local coordinates.

- Rhombohedral Phase:

In the rhombohedral unit cell, the polarization direction aligns with the [111] axis, which serves as the principal axis of the trigonal lattice. The rhombohedral unit cell undergoes shear

distortions, and the spontaneous strain is determined by the ratio of periodicity magnitudes along the $[111]$ and $[11\bar{1}]$ crystallographic directions. Mathematically, it is expressed as:

$$\varepsilon_0^R = \frac{9}{8} \left[\frac{R_{[111]}}{R_{[11\bar{1}]}} - 1 \right] \quad (3)$$

2.3. *Switching Mechanisms*

- **Tetragonal-Tetragonal Switching** (6 possible switching cases): This includes 90-degree and 180-degree domain switches within the tetragonal phase. 90-degree switching results in strain reorientation and significant changes in electromechanical response. 180-degree switching occurs without strain reorientation but reverses polarization direction.
- **Rhombohedral-Rhombohedral Switching** (8 possible switching cases): Domain switch occurs between the 8 different (111) variants. Switching mechanisms include 71-degree and 109-degree domain switches.
- **Interphase Switching**: The transformation between tetragonal and rhombohedral phases occurs under specific mechanical and electrical loading conditions. Unlike domain switching, interphase switching involves a lattice structure change, leading to higher energy barriers.

A crystallite is assumed to switch when the reduction of its potential energy exceeds a critical threshold:

$$-\Delta U \geq V_c \Delta \Psi_c \Rightarrow -\frac{\Delta U}{V_c} \geq \Delta \Psi_c \quad (4)$$

where ΔU is the change of potential energy due to switching, V_c is the volume of the switching crystallite and Ψ_c is the energy barrier per unit volume that resists the switch.

2.4. *Energy Considerations and the Inclusion Model*

Each crystallite is modeled as a spherical inclusion embedded in a homogeneous polycrystalline matrix subjected to an applied electric field E_i^∞ and stress σ_{ij}^∞ . The inclusion is constrained by the surrounding matrix, which already possesses a remanent strain ε_{ij}^{rm} and remanent polarization P_i^{rm} , reflecting prior switching events.

The total potential energy of the inclusion is given as:

$$U = U_0 + U_I \quad (5)$$

where U_0 represents the initial state of the inclusion within the matrix, and U_I is the interaction energy due to switching. The inclusion undergoes a transformation strain $\Delta\varepsilon_{ij}^t$ and polarization change ΔP_i^t , leading to an energy change, $U_I + \Delta U$, where:

$$\begin{aligned} \Delta U = V_I \left[-\sigma_{ij}^\infty \Delta\varepsilon_{ij}^t - E_i^\infty \Delta P_i^t + \frac{(7-5\nu)Y}{15(1-\nu^2)} \left(\varepsilon_{ij}^s - \varepsilon_{ij}^{rm} + \frac{1}{2} \Delta\varepsilon_{ij}^t \right) \Delta\varepsilon_{ij}^t \right. \\ \left. + \frac{1}{3\kappa} \left(P_i^s - P_i^{rm} + \frac{1}{2} \Delta P_i^t \right) \Delta P_i^t \right] \end{aligned} \quad (6)$$

The first two terms represent the driving forces for switching, corresponding to the mechanical work (stress-induced energy contribution) and electrical work (electric field-induced polarization change). The last two terms act as penalty terms, incorporating the mechanical mismatch energy and the electrical (depolarization-field) mismatch energy. The mechanical mismatch penalty quantifies the elastic energy cost associated with lattice deformation during switching, while the electrical mismatch penalty represents the interfacial energy barrier arising from polarization discontinuities between domains of different phases. These penalties impose energetic constraints that resist spontaneous switching, ensuring stability of the ferroelectric phase under applied mechanical and electrical loads. V_I represents the volume of the spherical inclusion.

2.5. Domain switching Criterion

A crystallite is assumed to switch when the reduction of its potential energy exceeds a critical threshold, given by Eqn. 4. The expression for ΔU (Eqn. 6) can be substituted in Eqn. 4 to obtain the switching criterion:

$$\sigma_{ij}^\infty \Delta\varepsilon_{ij}^t + E_i^\infty \Delta P_i^t - \frac{(7-5\nu)Y}{15(1-\nu^2)} \left(\varepsilon_{ij}^s - \varepsilon_{ij}^{rm} + \frac{1}{2} \Delta\varepsilon_{ij}^t \right) \Delta\varepsilon_{ij}^t - \frac{1}{3\kappa} \left(P_i^s - P_i^{rm} + \frac{1}{2} \Delta P_i^t \right) \Delta P_i^t \geq \Delta\Psi_c \quad (7a)$$

$$\alpha \left[\sigma_{ij}^\infty - \frac{(7-5\nu)Y}{15(1-\nu^2)} \left(\varepsilon_{ij}^s - \varepsilon_{ij}^{rm} + \frac{1}{2} \Delta\varepsilon_{ij}^t \right) \right] \Delta\varepsilon_{ij}^t + \left[E_i^\infty - \frac{1}{3\kappa} \left(P_i^s - P_i^{rm} + \frac{1}{2} \Delta P_i^t \right) \right] \Delta P_i^t \geq \Delta\Psi_c \quad (7b)$$

$$\alpha \left[\sigma_{ij}^\infty - \frac{2}{5} \bar{Y} \left(\varepsilon_{ij}^s - \varepsilon_{ij}^{rm} + \frac{1}{2} \Delta\varepsilon_{ij}^t \right) \right] \Delta\varepsilon_{ij}^t + \left[E_i^\infty - \frac{1}{3\kappa} \left(P_i^s - P_i^{rm} + \frac{1}{2} \Delta P_i^t \right) \right] \Delta P_i^t - \Delta\Psi_c \geq 0 \quad (7c)$$

As in Hwang *et al.*'s work, the parameter α (Eqn. 7b) serves as a weighting factor that distinguishes between mechanically driven and electrically driven switching. A value of $\alpha > 1$ is selected to favor stress-induced switching, ensuring that mechanical contributions are emphasized. The terms \bar{Y} and $\bar{\kappa}$ (Eqn. 7c) represent an effective modulus and effective dielectric permittivity. Poisson's ratio is approximated as 1/2, leading to the numerical factor 2/5 in Equation (7c).

The present model is developed based on thermodynamic energy minimization principles and assumes that switching occurs instantaneously when the energy barrier is exceeded. However, in reality, the switching process is rate-dependent, governed by domain wall motion kinetics and relaxation effects. Domain switching in ferroelectric ceramics involves nucleation and growth of domains, influenced by defect structures, local stress fields, and thermal activation. The dynamics of domain wall motion follow a viscoelastic response, where domain walls experience drag forces due to interactions with lattice defects and grain boundaries. Consequently, switching is not purely energy-driven but also time-dependent, requiring consideration of kinetic factors such as: Domain wall mobility, Pinning effects, Activation energy barriers. For interphase switching, the transformation from rhombohedral to tetragonal structures may exhibit additional time-dependent behavior due to the need for lattice reconfiguration.

The dielectric permittivity, piezoelectric coefficient, and elasticity tensors in general are anisotropic with the polar axis determining the symmetries. However, as in Hwang *et al.*'s work, the problem is simplified by assuming κ and s to be isotropic and the same for every crystallite given by

$$\kappa_{ij} = \kappa \delta_{ij} \quad (8a)$$

$$s_{ijkl} = \frac{1 + \nu}{Y} \delta_{ik} \delta_{jl} - \frac{\nu}{Y} \delta_{ij} \delta_{kl} \quad (8b)$$

The piezoelectric strain coefficient tensor for each crystallite is also simplified and details are provided in the next Section.

3. Model Implementation

The simulation begins with the material in a stress-free state (i.e., zero external load). A representative ensemble of crystallites is generated, where each crystallite is assigned either a

tetragonal or rhombohedral symmetry. This phase assignment reflects experimentally observed coexistence of tetragonal and rhombohedral domains at compositions near the MPB^{22,40}, which is known to yield superior piezoelectric properties due to multiple polarization reorientation pathways. In this numerical study, we assume a 50% rhombohedral-50% tetragonal composition.

3.1. Initialization and Phase Assignment

The simulation commences with an ensemble of crystallites, each assigned a phase—tetragonal or rhombohedral—based on the material composition relative to the MPB. The spontaneous polarization and spontaneous strain tensors are defined accordingly:

Tetragonal Phase:

$$\mathbf{P}^s(1) = -\mathbf{P}^s(2) = \begin{bmatrix} 0 \\ 0 \\ 1 \end{bmatrix}; \mathbf{P}^s(3) = -\mathbf{P}^s(4) = \begin{bmatrix} 1 \\ 0 \\ 0 \end{bmatrix}; \mathbf{P}^s(5) = -\mathbf{P}^s(6) = \begin{bmatrix} 0 \\ 1 \\ 0 \end{bmatrix} \quad (9a)$$

$$\begin{aligned} \varepsilon^s(1) = \varepsilon^s(2) &= \frac{1}{2}\varepsilon_0^T \begin{bmatrix} -1 & 0 & 0 \\ 0 & -1 & 0 \\ 0 & 0 & 2 \end{bmatrix}; \varepsilon^s(3) = \varepsilon^s(4) = \frac{1}{2}\varepsilon_0^T \begin{bmatrix} 2 & 0 & 0 \\ 0 & -1 & 0 \\ 0 & 0 & -1 \end{bmatrix}; \varepsilon^s(5) = \varepsilon^s(6) \\ &= \frac{1}{2}\varepsilon_0^T \begin{bmatrix} -1 & 0 & 0 \\ 0 & 2 & 0 \\ 0 & 0 & -1 \end{bmatrix} \end{aligned} \quad (9b)$$

Rhombohedral Phase:

$$\mathbf{P}^s(1) = -\mathbf{P}^s(2) = \frac{1}{\sqrt{3}} \begin{bmatrix} 1 \\ 1 \\ 1 \end{bmatrix}; \mathbf{P}^s(3) = -\mathbf{P}^s(4) = \frac{1}{\sqrt{3}} \begin{bmatrix} 1 \\ -1 \\ 1 \end{bmatrix}; \mathbf{P}^s(5) = -\mathbf{P}^s(6) = \frac{1}{\sqrt{3}} \begin{bmatrix} -1 \\ 1 \\ 1 \end{bmatrix}; \mathbf{P}^s(7) = -\mathbf{P}^s(8) = \frac{1}{\sqrt{3}} \begin{bmatrix} 1 \\ 1 \\ -1 \end{bmatrix} \quad (10a)$$

$$\begin{aligned} \varepsilon^s(1) = \varepsilon^s(2) &= \frac{1}{2}\varepsilon_0^R \begin{bmatrix} 0 & 1 & 1 \\ 1 & 0 & 1 \\ 1 & 1 & 0 \end{bmatrix}; \varepsilon^s(3) = \varepsilon^s(4) = \frac{1}{2}\varepsilon_0^T \begin{bmatrix} 0 & -1 & 1 \\ -1 & 0 & -1 \\ 1 & -1 & 0 \end{bmatrix}; \varepsilon^s(5) = \varepsilon^s(6) \\ &= \frac{1}{2}\varepsilon_0^T \begin{bmatrix} 0 & -1 & -1 \\ -1 & 0 & 1 \\ -1 & 1 & 0 \end{bmatrix}; \varepsilon^s(7) = \varepsilon^s(8) = \frac{1}{2}\varepsilon_0^T \begin{bmatrix} 0 & 1 & -1 \\ 1 & 0 & -1 \\ -1 & -1 & 0 \end{bmatrix} \end{aligned} \quad (10b)$$

3.2. Euler Angle Representation and Tensor Transformations

Each crystallite is embedded within a local coordinate system, which is oriented relative to the global Cartesian reference frame using the Z-X-Z convention of Euler angles (α, β, γ) , Fig. 1a. The corresponding transformation matrices for each individual rotation (Eqn. 11a) and the overall transformation matrix relating the local and global coordinate systems (Eqn. 11b) are given by:

$$R_z(\alpha) = \begin{bmatrix} \cos \alpha & -\sin \alpha & 0 \\ \sin \alpha & \cos \alpha & 0 \\ 0 & 0 & 1 \end{bmatrix}; R_x(\beta) = \begin{bmatrix} 1 & 0 & 0 \\ 0 & \cos \beta & -\sin \beta \\ 0 & \sin \beta & \cos \beta \end{bmatrix}; R_z(\gamma) = \begin{bmatrix} \cos \gamma & -\sin \gamma & 0 \\ \sin \gamma & \cos \gamma & 0 \\ 0 & 0 & 1 \end{bmatrix} \quad (11a)$$

$$\mathbf{R} = R_{z-x-z} = R_z(\gamma) R_x(\beta) R_z(\alpha) = \begin{bmatrix} \cos \alpha \cos \gamma - \cos \beta \sin \alpha \sin \gamma & -\cos \alpha \sin \gamma - \cos \beta \sin \alpha \cos \gamma & \sin \alpha \sin \beta \\ \sin \alpha \cos \gamma + \cos \beta \cos \alpha \sin \gamma & -\sin \alpha \sin \gamma + \cos \beta \cos \alpha \cos \gamma & -\cos \alpha \sin \beta \\ \sin \beta \sin \gamma & \sin \beta \cos \gamma & \cos \beta \end{bmatrix} \quad (11b)$$

Using this transformation, the global representation of the spontaneous strain and polarization tensors are obtained as:

$$\boldsymbol{\varepsilon}' = \mathbf{R} \boldsymbol{\varepsilon} \mathbf{R}^T; \mathbf{P}' = \mathbf{R} \mathbf{P} \quad (12)$$

3.3. Engineering Crystallographic Texture in Materials

Fig. 1b illustrates 3D spherical representations of the {001}, {100}, and {111} crystallographic textures, highlighting the spatial arrangement of key crystallographic planes and directions. These visualizations are essential for understanding how controlled orientation distributions influence domain switching under electrical and mechanical loading, as discussed in Section 4. The projections highlight key angular relationships, such as the 54.7° and 70.5° angles between different crystallographic directions, which play a critical role in determining the electromechanical response of piezo ceramics.

By selecting specific Euler angles (as detailed in Section 4), tailored textures can be engineered within the material to optimize electromechanical properties. By systematically controlling these orientations, materials can be designed with enhanced functional properties, ensuring preferred domain switching mechanisms for improved performance.

3.4. Piezoelectric Strain Tensor

The piezoelectric strain tensor, d_{ijk} describes the relationship between the induced strain and the applied electric field. In Voigt notation, the indices are reduced from three to two indices with the first index relating to electric field direction (1–3) and the second index relating to strain components ((1–6), with 4, 5, and 6 indices corresponding to 23, 13, and 12 shear components). In the phenomenological thermodynamic model of Haun *et al.*⁴⁰, the piezoelectric coefficients are

derived from electrostrictive relations rather than directly imposed symmetry constraints. This approach considers the coupling between strain and polarization, leading to a set of expressions for tetragonal and rhombohedral PZT.

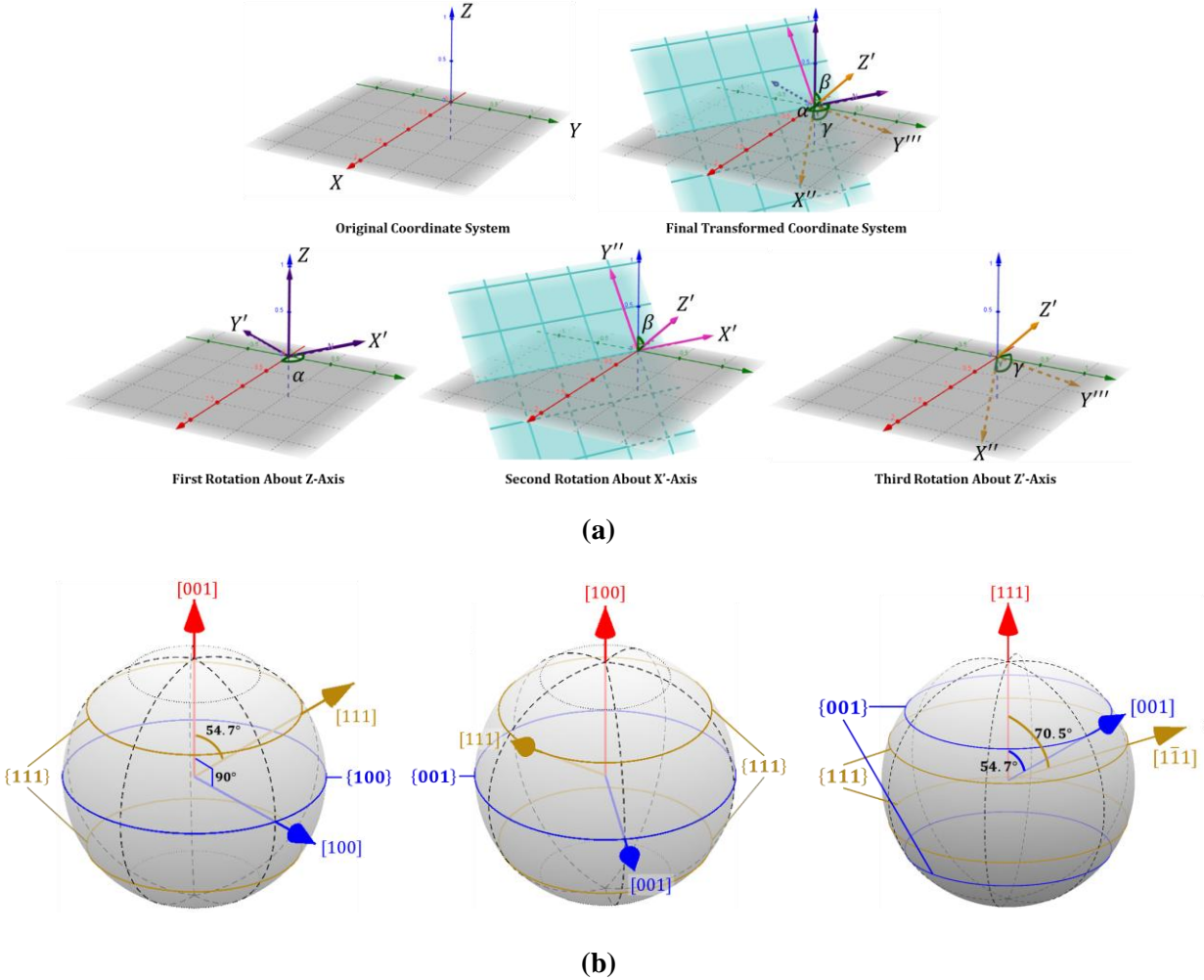


Figure 1. (a) Euler Angles to describe the orientation with respect to a fixed coordinate system. For this study we are using the Z-X-Z rotation scheme. Images adapted from GeoGebra⁴¹ (b) 3D spherical representations of the {001}, {100}, and {111} crystallographic textures. Note that the angles mentioned here (54.7°, 70.5°, and 90°) are for cubic symmetry. The angles in tetragonal and rhombohedral symmetry will be slightly different from these angles because of lattice distortion.

For tetragonal PZT, the derived piezoelectric coefficients are expressed in matrix form in Eqn. 13. For rhombohedral PZT, the spontaneous polarization aligns along the [111] direction, leading to a different set of coefficients. Table 1 shows the values of the d_{mn} components as a function of composition. Unlike tetragonal PZT, where d_{33} is maximized along [001] (the

spontaneous polarization direction), the maximum effective d_{33} in rhombohedral PZT occurs at an angle $\sim 59.4^\circ$ from $[111]$, rather than along the spontaneous $[111]$ polarization direction.

$$d_{mn}^{tetragonal} = \begin{bmatrix} 0 & 0 & 0 & 0 & d_{15} & 0 \\ 0 & 0 & 0 & d_{15} & 0 & 0 \\ d_{31} & d_{31} & d_{33} & 0 & 0 & 0 \end{bmatrix} \quad (13a)$$

$$d_{mn}^{rhombohedral} = \begin{bmatrix} d_{33} & d_{31} & d_{31} & d_{14} & d_{15} & d_{15} \\ d_{31} & d_{33} & d_{31} & d_{15} & d_{14} & d_{15} \\ d_{31} & d_{31} & d_{33} & d_{15} & d_{15} & d_{14} \end{bmatrix} \quad (13b)$$

Table 1: Theoretical piezoelectric coefficients as a function of composition at 25°C ⁴⁰

Tetragonal (40/60) [40% PbZrO ₃ & 60% PbTiO ₃] (pC/N or pm/V)	Rhombohedral (60/40) [60% PbZrO ₃ & 40% PbTiO ₃] (pC/N or pm/V)	MPB (50/50) [50% PbZrO ₃ & 50% PbTiO ₃] (pC/N or pm/V)	
		Tetragonal	Rhombohedral
$d_{33}=162$	$d_{33}=189$	$d_{33}=327$	$d_{33}=624$
$d_{15}=169$	$d_{15}=60$	$d_{15}=624$	$d_{15}=150$
$d_{31}=-58.5$	$d_{14}=-25.1$	$d_{31}=-156$	$d_{14}=-110$
	$d_{31}=-80.5$		$d_{31}=-310$

The transformation of the third-rank piezoelectric strain tensor d_{ijk} follows the standard tensor transformation rule: $d'_{pqr} = A_{pi}A_{qj}A_{rk}d'_{ijk}$, where A is the coordinate transformation matrix that maps from the initial to the new coordinate system. The d_{mn} components given in Table 1 are with respect to a coordinate system whose Z-direction coincides with the $[001]$ direction for both tetragonal and rhombohedral symmetry. In contrast, in Du et al.'s work⁴², for tetragonal symmetry, the Z-axis aligned along $[001]$, whereas for rhombohedral symmetry, the Z-axis is assumed to align with $[111]$.

It is important to note that despite the inherent lattice distortions in the rhombohedral system, the same transformation equation is applied under the assumption that these deviations are small enough to justify treating the transformation as if it were Cartesian, simplifying the analysis while maintaining reasonable accuracy.

Figure 2(a, b) illustrates the variation of d_{33} for tetragonal and rhombohedral 40/60 PZT crystals. In the tetragonal phase, d_{33} reaches its maximum value of 162 pC/N along the polarization

direction [001], while in the [111] direction, it decreases to 74 pC/N. The behavior of d_{33} in the rhombohedral phase exhibits a different trend. Instead of peaking along the polarization direction [111], the maximum occurs approximately 56.7° away from it, a direction equivalent to [001] in perovskites. For rhombohedral 40/60 crystals, d_{33} attains a maximum of 189 pC/N along the three [001] directions, while along the [111] directions, it is significantly lower at 71 pC/N. At the morphotropic phase boundary (MPB), the piezoelectric response is further enhanced, Fig. 2(c, d) with tetragonal crystals exhibiting a peak d_{33} value of 327 pC/N along [001], whereas for rhombohedral crystals, the maximum value increases to 624 pC/N along [001].

The phenomenological model of piezoelectric coefficients successfully captures the enhanced electromechanical properties near the MPB⁴³, making it useful for optimizing texture-dependent piezoelectric performance in this study.

3.5. *Incremental Loading and Switching Criterion*

The model employs an incremental loading scheme where an external field—electrical, mechanical, or a combination—is applied in small steps, ensuring that only a limited number of crystallites switch at each stage. After each load increment, every crystallite is evaluated against the switching criterion, Eqn. 7, to determine whether a phase transformation occurs. Figure 3 presents the numerical procedure in a flowchart. The simulation begins by defining the number of crystallites, phase fractions, and incremental loading steps. Using MATLAB’s random number generator, Euler angles are assigned to each crystallite, ensuring a particular texture in the material and a representative mixture of tetragonal and rhombohedral phases characteristic of the MPB.

As the load is gradually increased, the system allows incremental switching of crystallites, mirroring real material behavior. The switching process follows energy minimization principles, evaluating all potential switching pathways and selecting the one that maximizes the driving force. The coercive field for interphase switching is typically higher than that for intra-phase switching. As a result, interphase switching at the MPB is prioritized once the coercive field for interphase switching is exceeded, playing a crucial role in enhancing material response.

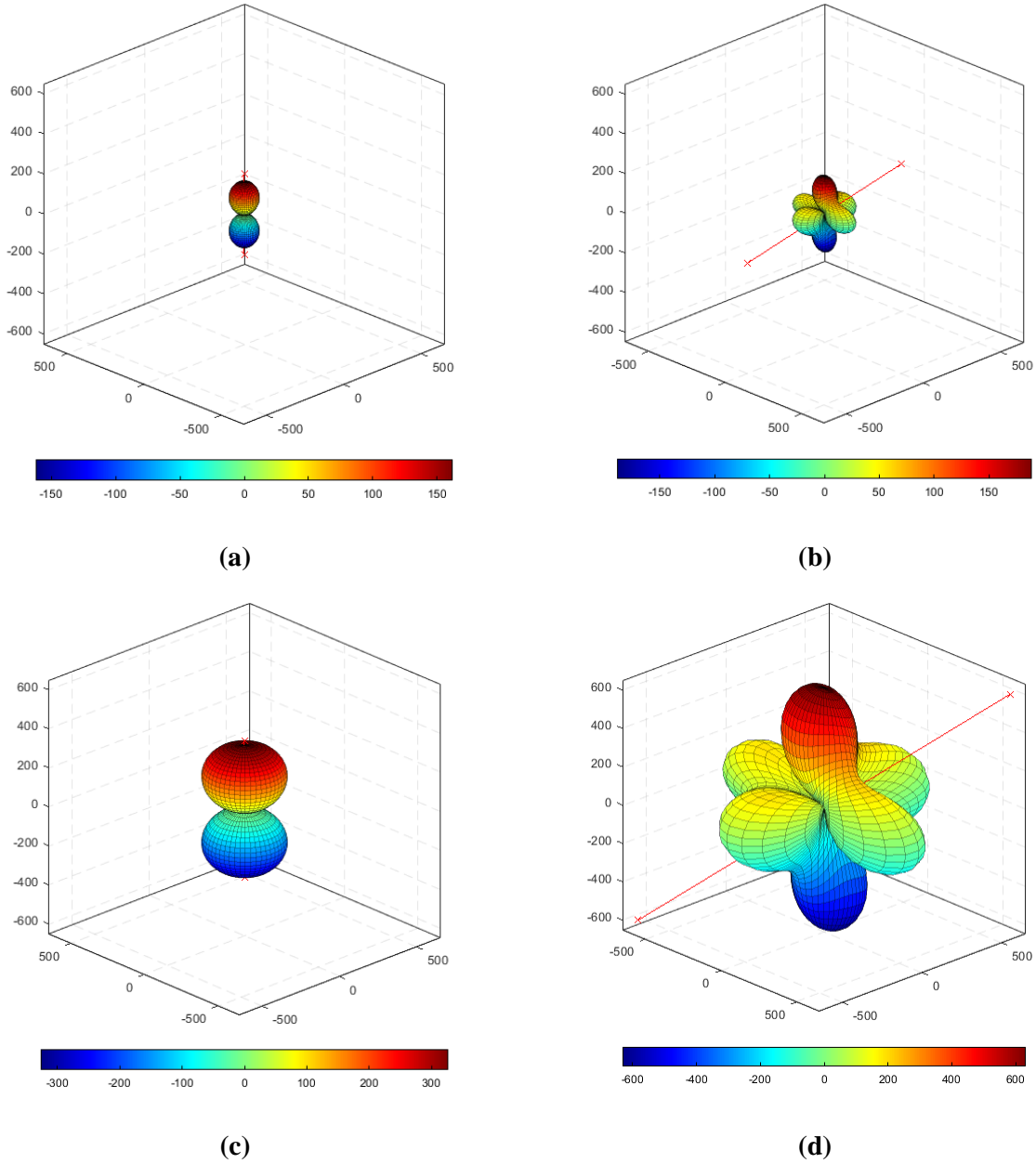


Figure 2. Representation of the d_{33} surface along the [001] direction for different PZT compositions: **(a)** Tetragonal (40/60) unit cells, **(b)** Rhombohedral (60/40) unit cells, **(c)** Tetragonal (50/50) unit cells at the MPB composition, and **(d)** Rhombohedral (50/50) unit cells at the MPB composition.

Once all permissible switches are executed, the macroscopic remanent strain (ϵ_{rm}) and remanent polarization (P_{rm}) are computed by averaging over all crystallites. These values are updated iteratively, permitting additional switching without further load increments, until no further switching occurs.

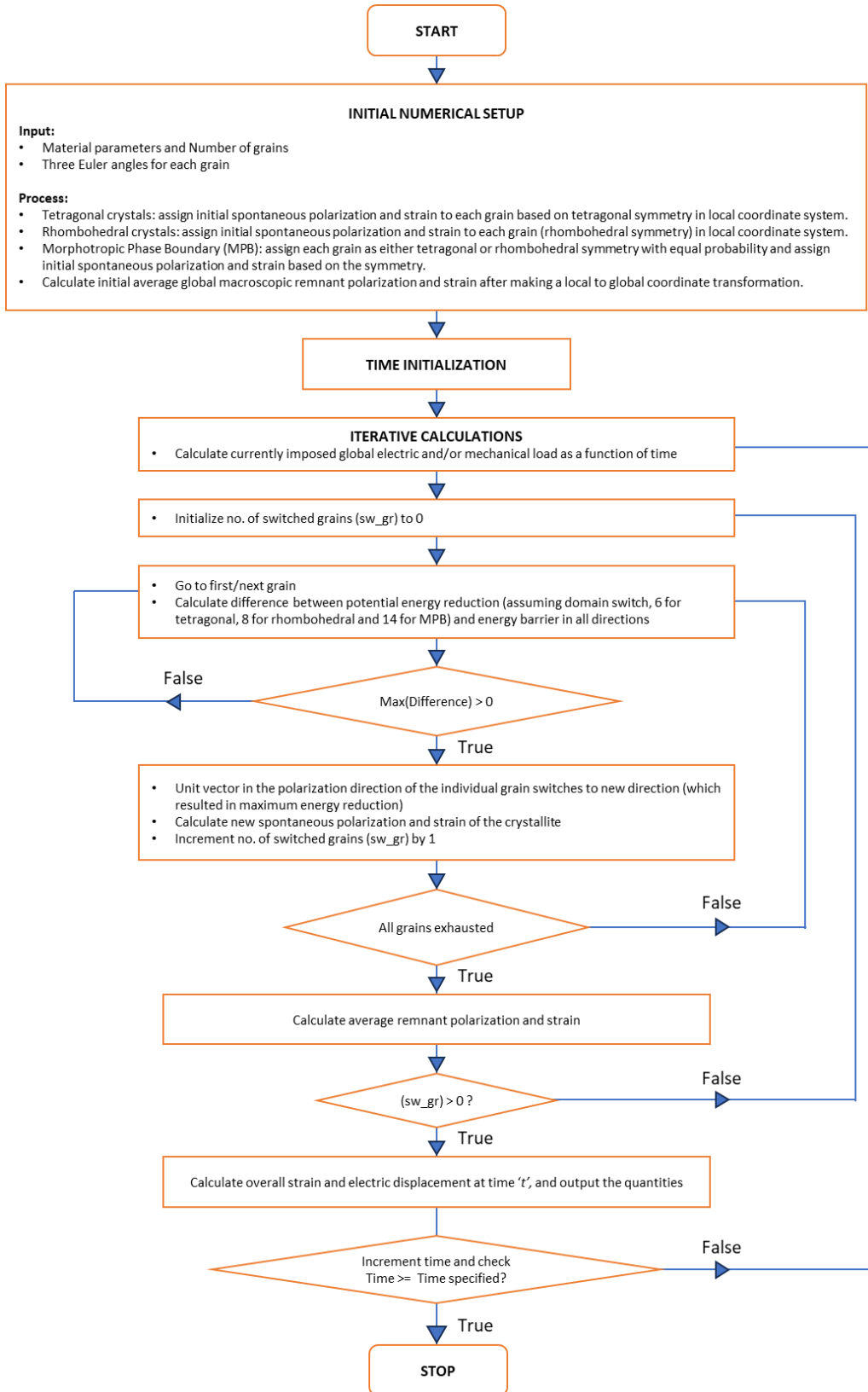


Figure 3. Flowchart illustrating the implementation of the numerical model.

Subsequently, the linear contributions to strain and electric displacement are calculated for each crystallite using the elastic compliance and dielectric permittivity tensors, incorporating phase-specific tensor components for tetragonal and rhombohedral symmetries. The final macroscopic electric displacement and strain are obtained as a volume average over all crystallites, capturing the enhanced electromechanical coupling induced by the interplay of tetragonal and rhombohedral phases. The results offer insights into the mechanisms driving superior piezoelectric performance.

4. Results and Discussion

4.1. Fitting Parameters

The fitting parameters used in this study, as detailed in Table 2, were sourced from Refs. [29,35,39], where they were derived by aligning numerical simulations with experimental data for polycrystalline ceramics. Several key considerations guided the parameter selection. The coercive field for intraphase 71° and 109° switching was set to half that of intraphase 90° switching, consistent with experimental observations in Ref. [35]. Additionally, the spontaneous polarization ratio between rhombohedral and tetragonal phases was maintained as reported in Ref. [35] to ensure consistency with prior studies. The piezoelectric coefficients (d_{ijk}) were scaled to ten times the values listed in Table 1, as Hwang *et al.*²⁹ used values an order of magnitude higher in their study. The primary focus of this work is not on parameter optimization but rather on understanding the mechanics of domain switching and elucidating the role of texturing in shaping the electromechanical response. Therefore, a direct fitting of the model to PZT experimental data has been conducted at the end of this section to validate the numerical predictions.

4.2. Validation of Numerical Scheme

To verify the correctness of the numerical implementation, the model was initially tested for tetragonal symmetry using the parameters specified in Table 2 and $d_{33} = 2.376 \times 10^{-9}$ m/V and $d_{31} = -0.5d_{33}$ and $d_{15} = 0$. The results presented in Figures 4(a) and 4(b) closely match those reported by Hwang *et al.*²⁹.

Figure 4(a) shows the electric displacement (D_3) as a function of the applied electric field (E_3), starting from an unpoled state (random orientation). The numerical simulations were

performed with 5000 crystallites, and the hysteresis loop stabilizes after completing a full cycle. The remanent polarization and strain of the ceramic, computed as the average of the crystallite spontaneous polarizations and strains, are zero at the start of the simulation. The inset labeled *A* illustrates the initial random polarization state of the crystallites, where each red dot represents the tip of a polarization vector originating from the center, forming a sphere of radius P_0 . As the electric field increases from zero, the electric displacement gradually rises due to the dielectric effect, marking the transition from *A* to *B*. At *B*, a sharp increase in electric displacement occurs due to domain switching, leading to poling of the material. The remanent polarization nearly saturates at *C*, where the inset shows that the polarization vectors cluster near the upper pole. Upon decreasing the field from *C*, the electric displacement follows a nearly linear decline until a sudden drop occurs at *D*, corresponding to reverse domain switching (depolarization). As the field continues decreasing, the remanent polarization approaches negative saturation at *E*, where the polarization vectors cluster around the lower pole (inset *E*). When the field is increased again, a sharp jump back to positive electric displacement is observed at *F*, completing the cycle.

Table 2. Parameters used in numerical simulation.

Parameter	Description	Value [Reference]
\bar{E}_0^{90}	Effective coercive field for intraphase 90° switch	0.13 MV/m ²⁹
\bar{E}_0^{180}	Effective coercive field for intraphase 180° switch	1.0 MV/m ²⁹
$\bar{E}_0^{71,109}$	Effective coercive field for intraphase 71° and 109° switch	0.064 MV/m ³⁵
$\bar{E}_0^{55,125}$	Effective coercive field for interphase 55° and 125° switch	0.5 MV/m
$\bar{\kappa}$	Effective dielectric permittivity	0.80 $\mu\text{F}/\text{m}^{29}$
\bar{Y}	Effective elastic modulus	7.5 GPa ²⁹
P_0	Spontaneous polarization	0.3 C/m ² ²⁹
ε_0^T	Spontaneous strain (tetragonal)	0.0028 ²⁹
ε_0^R	Spontaneous strain (rhombohedral)	0.0023 ³⁵
α	Weight Parameter	1.4 ²⁹
d_{ijk}	Piezoelectric strain coefficient	[Table 1 \times 10] ²⁹
N	Number of Crystallites	5000 ²⁹

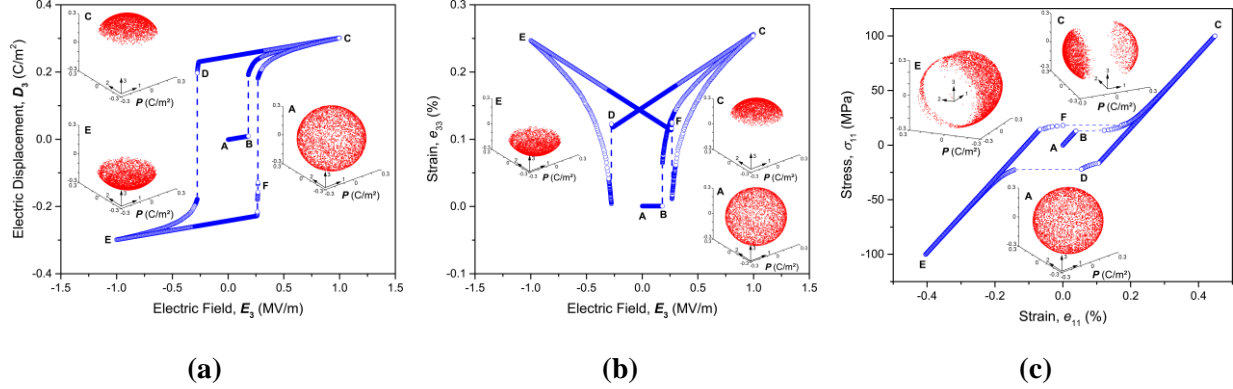


Figure 4. (a) Simulated electric displacement (D_3) vs. electric field (E_3) hysteresis loop under zero applied stress. (b) Simulated strain (e_{33}) vs. electric field (E_3) butterfly loop under zero applied stress. (c) Simulated stress (σ_{11}) vs. strain (e_{11}) hysteresis loop under zero applied electric field, where the loop begins with tensile stress rather than the conventional compressive stress. The material texture is random, and the insets illustrate polarization vector evolution: (A) spherical distribution at the start of the test, (C) polarization clustering along the top pole at maximum positive electric field, and (E) clustering along the bottom pole at maximum negative electric field.

Figure 4(b) presents the strain (e_{33}) as a function of the electric field (E_3), corresponding to the hysteresis behavior observed in Figure 4(a). Initially, the strain remains constant as the electric field increases from zero, indicating a nonpiezoelectric response due to the cancellation of piezoelectric contributions in the unpoled ceramic. At B , poling occurs, resulting in a sudden strain increase, which saturates at C . The strain curve follows a more gradual progression compared to electric displacement. When the electric field is reduced from C , the strain decreases linearly due to the piezoelectric effect, followed by a sharp drop at D , marking depolarization. Further reduction in the field leads to repolarization, with strain rising again to reach saturation at E . At this stage, the reversal of polarization alters the piezoelectric coefficients of the crystallites, leading to a sign change in the piezoelectric response. As the field increases again from E , the strain decreases linearly, and the cyclic process continues. The polarization vector distributions in the insets follow a similar trend to Figure 4(a).

Figure 4(c) depicts the average uniaxial stress (σ_{11}) versus strain (e_{11}) response under mechanical loading. Initially, as stress increases from zero, strain increases in accordance with linear elasticity. At B , 90° domain switching occurs, leading to a further increase in strain as tetragonal domains reorient, aligning their c -axes along the loading direction. At saturation point

C , the inset shows polarization vectors aligned along the loading axis. Upon reducing the stress from C , the strain decreases linearly due to elastic unloading, followed by a sharp transition at D , where compressive stress (σ_{11}) induces domain switching, causing a jump to negative strain. Saturation is reached at E , where the polarization vectors align perpendicular to the compressive loading direction (inset E). The cycle then repeats with further unloading and reloading.

4.3. *Polycrystalline Ferroelectric Model at the MPB Composition*

Now that we have validated the code to be working correctly, we proceed to simulate the ferroelectric response for rhombohedral symmetry and the response at the MPB composition. The MPB composition is of particular interest due to its enhanced electromechanical properties, which arise from the increased ease of polarization rotation and domain switching. In this sub-section, the electric and mechanical responses of these different phase compositions are compared under applied electric field and mechanical stress, highlighting the key differences in their polarization, strain, and stress-strain behavior.

Figure 5(a) illustrates the polycrystalline ferroelectric model used in the simulations. The schematic represents a three-dimensional polycrystalline structure, where individual crystallites are randomly oriented. The applied electric field (E_3) and mechanical stresses (σ_{11} , σ_{22} , σ_{33}) are indicated, along with the associated material responses, including electric displacement (D_3) and strain components (e_{11} , e_{22} , e_{33}). The numerical simulations track the evolution of polarization and strain under external electrical and mechanical stimuli, capturing the domain switching behavior in different crystallographic phases.

Figures 5(b) and 5(c) present the simulated hysteresis loops for electric displacement (D_3) and strain (e_{33}), respectively, as functions of the applied electric field (E_3) for three different ferroelectric phase compositions: tetragonal, rhombohedral, and MPB compositions. The tetragonal phase (blue dashed line) exhibits a sharp polarization switching response, characterized by a relatively higher coercive field and distinct polarization jumps. The corresponding butterfly-shaped strain response, similar to Figure 4(b), shows relatively lower strain magnitudes and a smaller strain-electric field slope (piezoelectric strain coefficient) due to the limited number of available domain switching pathways. The rhombohedral phase (red dotted line) demonstrates a more gradual polarization and strain response, attributed to multi-variant domain switching and a

lower coercive field. The slope of the strain-electric field curve is slightly larger than that of the tetragonal phase.

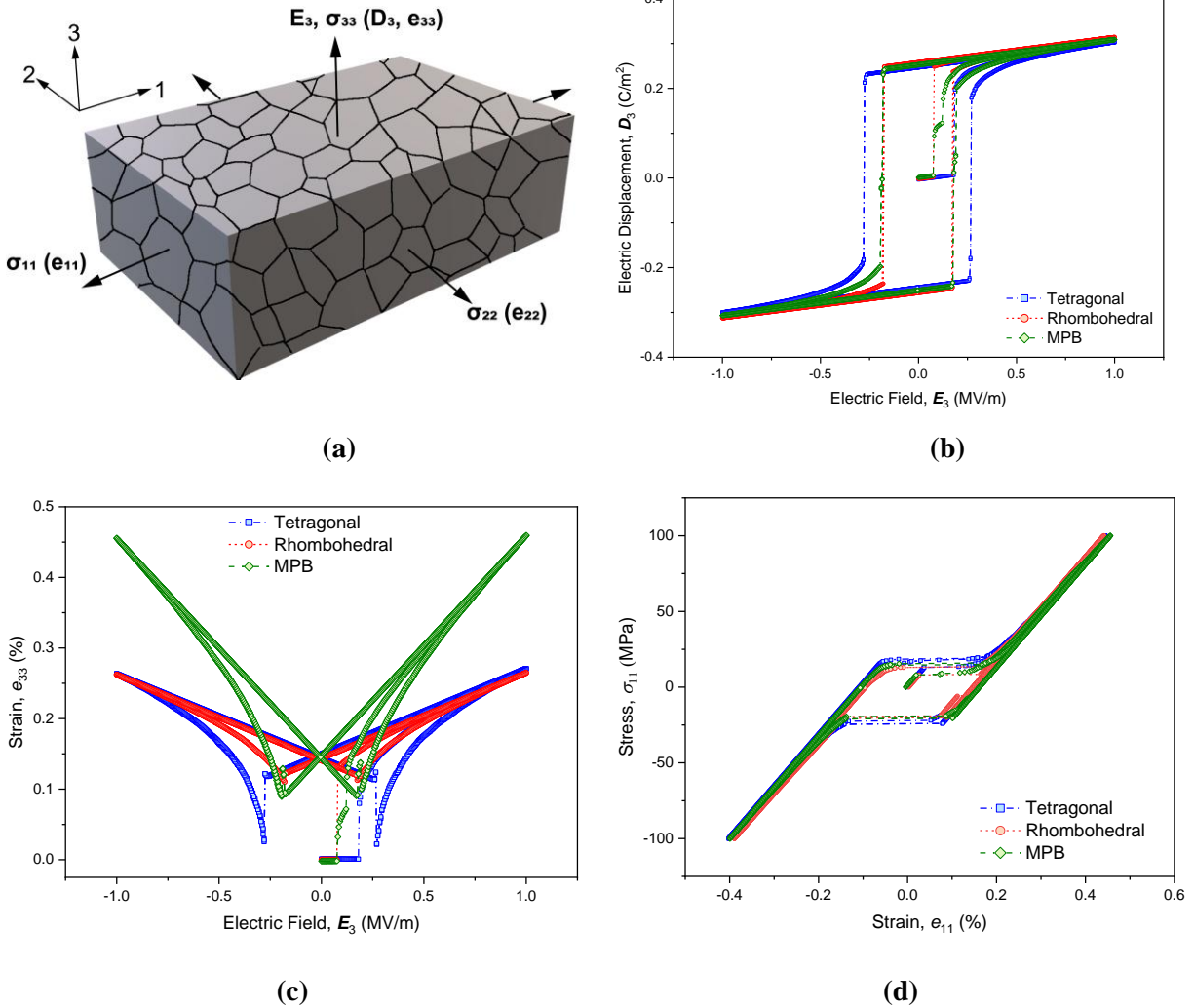


Figure 5. (a) Schematic representation of the polycrystalline ferroelectric model used in the simulations. (b) Simulated electric displacement (D_3) vs. electric field (E_3) hysteresis loops for tetragonal, rhombohedral, and morphotropic phase boundary (MPB) compositions, highlighting differences in polarization switching behavior. (c) Strain (e_{33}) vs. electric field (E_3) butterfly loops, showing enhanced strain response for the MPB composition due to facilitated domain reorientation. (d) Stress (σ_{11}) vs. strain (e_{11}) response under uniaxial loading for different phase compositions.

The MPB composition (green diamonds) exhibits enhanced polarization switching and the highest strain response among the three phases. This superior electromechanical performance is due to the coexistence of tetragonal and rhombohedral domains, which enables easier domain

reorientation under an applied electric field. The MPB composition also has the steepest strain-electric field slope, further highlighting its advantages for piezoelectric applications. These simulation results are in excellent agreement with experimental observations reported for polycrystalline PZT for these three phase compositions (see Fig. 4 in Ref. [35]). Also, the maximization of piezoelectric strain coefficient at the MPB composition has been well reported⁴³.

Figure 5(d) presents the mechanical response in terms of stress (σ_{11}) versus strain (e_{11}) under uniaxial loading for different phase compositions. The MPB composition exhibits the most gradual and smooth stress-strain response, attributed to the facilitated multi-variant domain reorientation. This behavior indicates that MPB materials provide an optimal balance between mechanical compliance and electromechanical coupling, reinforcing their significance in advanced actuator and sensor applications.

4.4. *Effect of Texture (or Crystallite Orientation) on the Electromechanical Response*

Researchers have extensively developed textured PZT ceramics and thin films to enhance piezoelectric performance by promoting crystallite alignment along favorable crystallographic directions, as documented in the Introduction Section. Fig. 6 presents the influence of different initial crystallographic texture orientations on the piezoelectric response of polycrystalline PZT at the MPB composition under applied electric and mechanical loading. The simulations are conducted for four distinct texture cases: (001)-oriented, (100)-oriented, (111)-oriented, and randomly oriented crystallites.

For a ceramic with (001) preferred orientation, the three Euler angles (α, β, γ) are generated using a MATLAB random number generator to simulate crystallite misalignment within the textured material. The angle α , representing in-plane rotation, is uniformly distributed between 0 and 2π . The tilt angle β follows a normal distribution centered at zero with a standard deviation of $\pi/30$ (a variable that controls the degree of texture sharpness, where a smaller standard deviation corresponds to better texture alignment). The out-of-plane rotation γ follows a normal distribution with a mean of 0, $\pi/2$, π , or $3\pi/2$ and a standard deviation of $\pi/30$.

For a (100) preferred orientation, the in-plane rotation α is uniformly distributed between 0 and 2π . The tilt angle β has a normal distribution with a mean of $\pi/2$ and a standard deviation of

$\pi/30$. The rotation angle γ is normally distributed around $\pi/2$ or $3\pi/2$ with a standard deviation of $\pi/30$.

For a (111) preferred orientation, α is again uniformly distributed between 0 and 2π . The tilt angle β follows a normal distribution centered at either $\cos^{-1}(1/\sqrt{3})$ or $\pi - \cos^{-1}(1/\sqrt{3})$ with a standard deviation of $\pi/30$. The out-of-plane rotation γ follows a normal distribution with a mean of $\pi/4$, $3\pi/4$, $5\pi/4$, or $7\pi/4$ and a standard deviation of $\pi/30$.

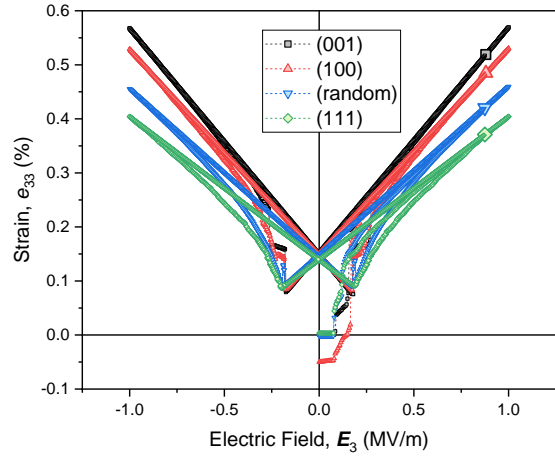
This approach ensures that the generated Euler angles maintain the appropriate degree of texture alignment while allowing for small misorientations, simulating real-world processing conditions where perfect texture is rarely achieved. Figures 6(a) and 6(b) illustrate the strain (e_{33} and e_{11}) responses as a function of the applied electric field (E_3), for different crystallographic textures, and for a standard deviation of $\pi/10$. The (001)-oriented crystallites (black curve) exhibit the highest strain response due to favorable domain switching mechanisms. The (100)-oriented crystallites (red curve) show an intermediate strain response, followed by the response from randomly oriented crystallites (blue curve) which combines contributions from various orientations. The (111)-oriented crystallites (green curve) exhibit the lowest strain response, as polarization rotation is less favorable in this orientation. The variation in strain response confirms that crystallite orientation significantly impacts the piezoelectric properties, with the (001) texture providing the most favorable electromechanical behavior.

Experimental and theoretical studies consistently confirm that the strain response of PZT is strongly dependent on crystallographic orientation, with (001)-oriented crystallites exhibiting the highest strain response, followed by (100), random, and (111)-oriented crystallites, which show the lowest response. Phenomenological modeling (Du *et al.*, 1998) predicts that the piezoelectric coefficient d_{33} —and consequently the strain e_{33} —is maximal along [001] and decreases as the crystal tilts toward [111]. Bulk templated grain growth (TGG) experiments show that textured (001) PZT ceramics exhibit up to $2\times$ larger strain than random polycrystals and significantly outperform (111) textures¹³. Similarly, in thin-film PZT, experimental studies^{14,44} demonstrate that (001)-textured films yield 50–60% higher piezoelectric strain than (111)-textured films, attributed to enhanced polarization alignment and domain switching. Recent work on freestanding PZT films by Das *et al.*¹⁰ confirms that strain and piezoelectric output systematically decrease from (001) to (111) orientations, with mixed textures exhibiting intermediate responses. These findings validate

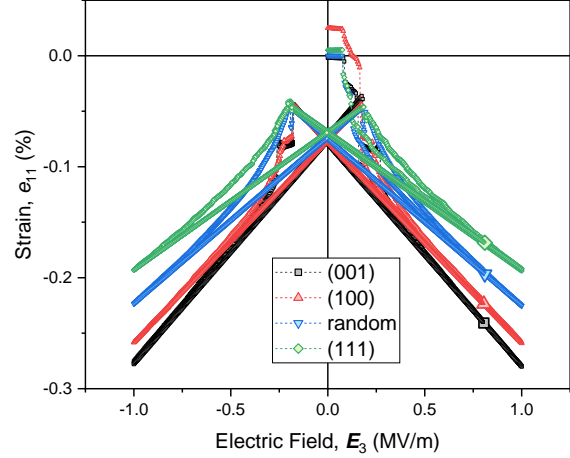
the model's prediction that crystallite orientation strongly influences electromechanical behavior, with (001) texture providing the most favorable strain response in both bulk and thin-film PZT.

Figure 6(c) presents the electric displacement (D_3) vs. applied electric field (E_3) hysteresis loops for different initial crystallite orientations. The results indicate that the (001)-textured ceramic exhibits wider hysteresis loops (measured as the loop width at zero displacement) compared to the (111)-textured ceramic. Additionally, polarization reversal in the (111) texture occurs more gradually, as evidenced by the smoother transition to saturation after each polarization switching event, in contrast to the sharper transitions to saturation observed in the (001) texture. This behavior suggests that domain switching dynamics are more continuous and distributed in (111)-oriented crystallites, whereas (001)-oriented crystallites undergo more abrupt polarization flips. Similar trends have been reported in PZT thin films with (001) preferential texture grown on Pt/MgO substrates, where stronger out-of-plane polarization and larger coercive fields were observed compared to randomly oriented or (111)-textured films ⁴⁵.

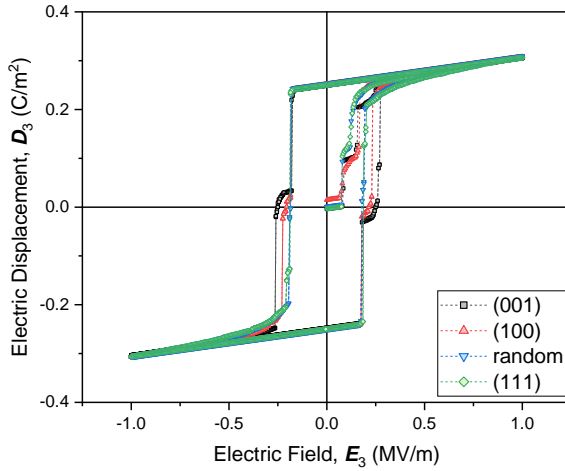
Figures 6(d) and 6(e) compare the effective piezoelectric coefficients (d_{33} and d_{31}) for different initial crystallite orientations. Among the various textures, the (001)- and (100)-oriented crystallites exhibit the highest values of d_{33} and d_{31} , and their responses are nearly identical when the standard deviation of misorientation is small. This similarity explains why many research studies do not distinguish between the (001) and (100) orientations, instead referring to them collectively as {100} or (100)/(001) texture ¹⁴. However, as the standard deviation increases, Fig. 6(d) and 6(e) indicate that d_{33} and d_{31} for (001)-textured crystallites remain higher than those for (100)-textured crystallites, suggesting that the 001-oriented domains retain stronger piezoelectric activity even with increasing misorientation. As a result, it is better to distinguish between (001) and (100) textures. In contrast, the (111)-oriented crystallites consistently exhibit the lowest values of d_{33} and d_{31} . Additionally, as the standard deviation increases, the values of d_{33} and d_{31} across all textures begin to converge, reflecting the fact that a high degree of misorientation effectively randomizes the crystallite orientations, reducing the benefits of texture alignment.



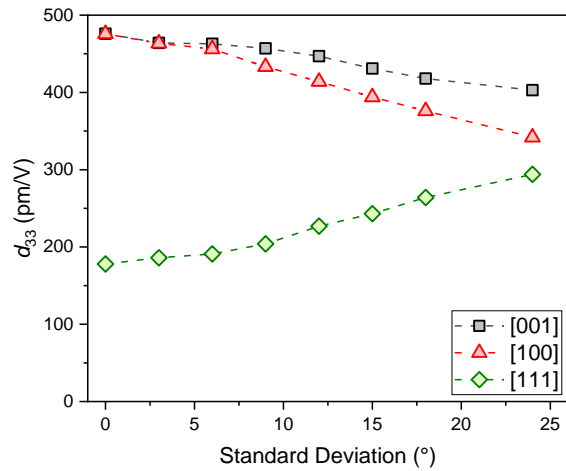
(a)



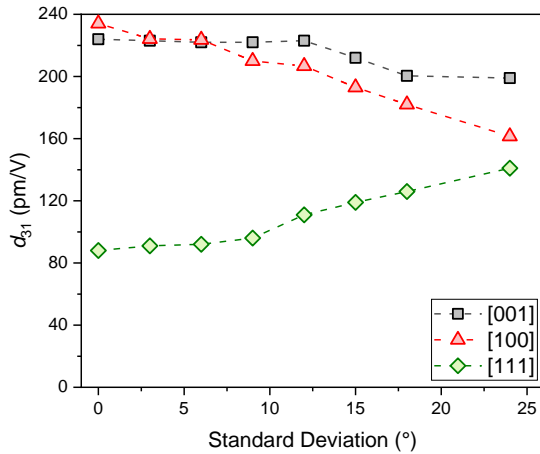
(b)



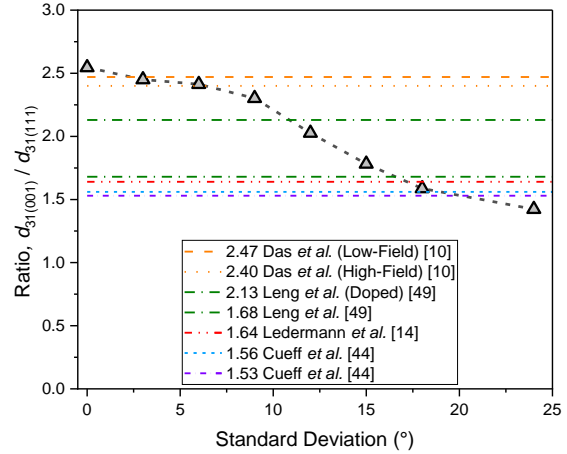
(c)



(d)



(e)



(f)

Figure 6: (a) Strain (e_{33}) vs. electric field (E_3) butterfly loops, illustrating that (001)-textured crystallites exhibit the highest strain response and slope (d_{33}), followed by (100), random, and (111) orientations. (b) Strain (e_{11}) vs.

electric field (E_3) butterfly loops. Note that (a) and (b) are constructed for a standard deviation of $\pi/10$ (c) Electric-displacement (D_3) vs. E_3 hysteresis loops. Comparison of effective piezoelectric coefficients (d) d_{33} and (e) d_{31} for different textures, showing that (001) and (100) orientations yield the highest values and with increasing standard deviation converge towards random orientation. (f) Ratio of piezoelectric coefficients (d_{33}/d_{31}) compared with experimental data, demonstrating that the model predicts a maximum theoretical ratio of ~ 2.6 , which decreases as misorientation increases, aligning well with reported experimental values.

A major challenge in evaluating piezoelectric coefficients in PZT ceramics is the significant variability in reported experimental data^{46,47}. This variability makes direct comparisons of absolute d_{33} and d_{31} values difficult. Therefore, Figure 6(f) presents a comparison of the ratio d_{33}/d_{31} instead, allowing for a more robust comparison with experimental data. The results indicate that the maximum attainable ratio in the model is ~ 2.6 , and as the standard deviation increases, this ratio gradually approaches $\rightarrow 1$, consistent with increasing crystallite misalignment. Experimentally reported values also align well with the model: the highest reported ratio in literature is 2.47^{10} , corresponding to freestanding PZT films with nearly 100% (001) and 100% (111) texture, where the authors estimate a standard deviation of $\sim 5^\circ$ from XRD measurements⁴⁸. Other reported ratios fall within the range of 1.53^{44} to 1.64^{14} , matching the model predictions at higher standard deviation values, indicative of less well-aligned crystallites. However, many experimental studies do not report the standard deviation of their texture measurements, a crucial parameter necessary for accurate comparison. Also, note the ratio of 2.13 and 1.68 for doped and non-doped textured PIN–PMN–PT ceramics⁴⁹, respectively.

In the next section, we will explore how residual stress also influences the measured d_{33}/d_{31} ratio. However, even when accounting for residual stress, the model predicts that the maximum theoretical ratio hardly exceeds 2.6, reinforcing the limits of texture-induced enhancement in polycrystalline PZT ceramics.

Fig. 7 illustrates the evolution of polarization vectors as an electric field is applied in ferroelectric ceramics with different crystallographic textures (001), (100), and (111), for three different phase compositions: morphotropic phase boundary (MPB), tetragonal, and rhombohedral. The polarization distributions are shown at three key points in the hysteresis/butterfly loop: A: Initial unpoled state (distribution before applying an external field).

C: Positive saturation (after applying a strong positive electric field). *E*: Negative saturation (after reversing the field to a strong negative value).

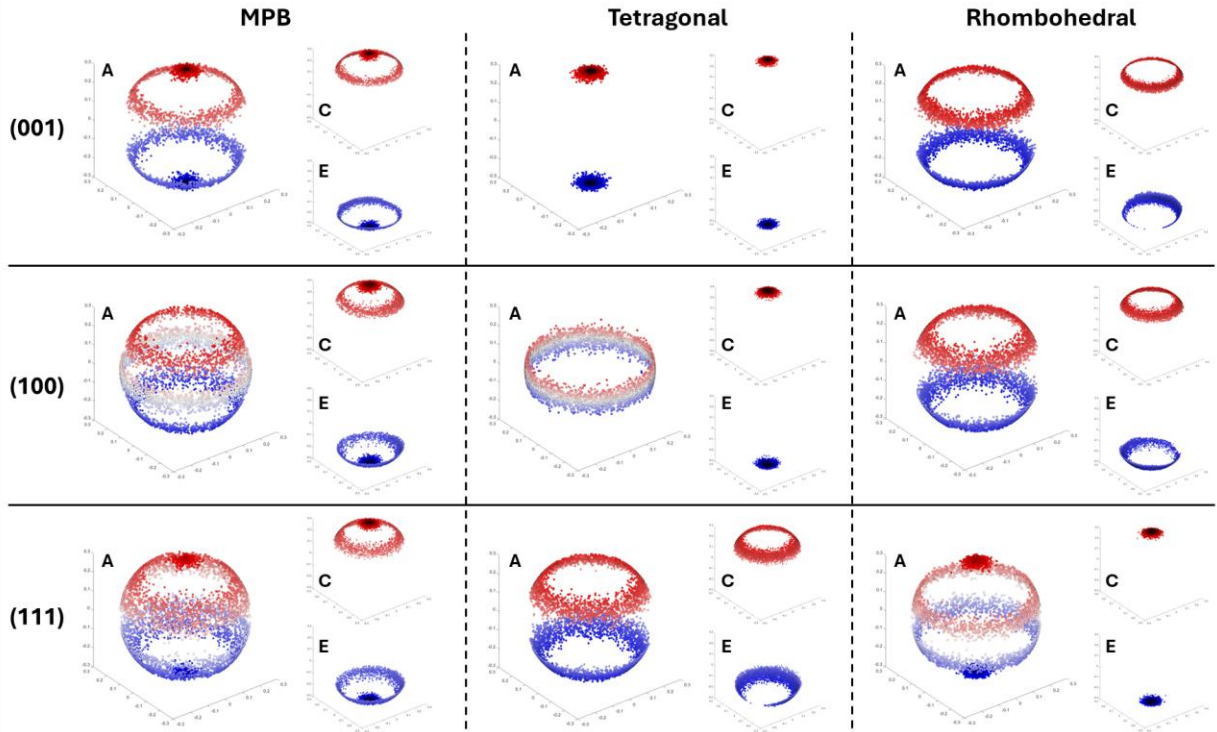


Figure 7. Evolution of polarization vectors at key points in the hysteresis/butterfly loop for different crystallographic textures (001), (100), and (111) and phase compositions (MPB, tetragonal, and rhombohedral phases). The subfigures labeled A, C, and E represent the initial unpoled state, positive saturation, and negative saturation, respectively. The differences in domain switching behavior across textures highlight the impact of crystallographic orientation on ferroelectric properties. The color scheme follows a red-blue gradient, transitioning from white at the equator to red at the north pole and white (equator) to blue at the south pole.

For (001)-Oriented Textured Crystallites: At A: The polarization vectors for the MPB composition are aligned along the top and bottom poles and along two rings at approximately 54.7° from the top and bottom poles (refer to Fig. 1(b)), reflecting the combination of tetragonal and rhombohedral symmetry. For tetragonal symmetry the polarization vectors cluster along the (001) directions whereas for rhombohedral symmetry the polarization vectors cluster along the (111) directions. At C: As the maximum positive electric field E_3 is applied, the polarization vectors align strongly along the field direction, leading to switching of domains to the top hemisphere. At

E: When the field is at its maximum negative value, the polarization vectors undergo a complete reversal, flipping to the bottom hemisphere.

For (100)-Oriented Textured Crystallites: At *A*: The polarization vectors for the MPB composition are aligned along the equator and along two rings at approximately 54.7° from the top and bottom poles (refer to Fig. 1(b)). This distribution results from the combination of tetragonal and rhombohedral domain structures, where tetragonal domains align along the (001) directions on the equatorial plane, while rhombohedral domains align along the (111) directions, forming the two additional rings. At *C*: As the maximum positive electric field E_3 is applied, the polarization vectors for the tetragonal symmetry flip towards the field direction clustering near the top pole, whereas in the rhombohedral symmetry, the polarization vectors from the bottom ring transition toward the top ring. At *E*: When the field is at its maximum negative value, the polarization vectors from the top pole and ring have flipped to the opposite hemisphere.

For (111)-Oriented Textured Crystallites: At *A*: The polarization vectors for the MPB composition exhibit a complex distribution due to the combined influence of tetragonal and rhombohedral symmetries. For tetragonal symmetry the polarization vectors cluster along the (001) directions which in this case are along two rings at approximately 54.7° from the top and bottom poles, whereas for rhombohedral symmetry the polarization vectors cluster along the (111) directions which in this case is along the top and bottom poles and along two rings at approximately 70.5° from the poles. At *C*: As the maximum positive electric field E_3 is applied, the polarization vectors for the tetragonal symmetry flip towards the field direction clustering near the top ring whereas for the rhombohedral symmetry the polarization vectors from the bottom pole, bottom ring, and top ring flip to the top pole. At *E*: When the field is at its maximum negative value, the polarization vectors from the top pole and ring (state *C* in the MPB case) have flipped to the opposite hemisphere.

These differences in polarization switching behavior highlight the strong influence of texture on domain reorientation and ferroelectric response, directly impacting the piezoelectric performance of polycrystalline materials.

4.5. *Effect of Stress (and Residual Stress) on Electromechanical Response*

Stress plays a critical role in domain switching and overall electromechanical behavior in ferroelectric and piezoelectric materials. In particular, residual stresses—which can reach several

hundred MPa^{12,26}—develop in sol-gel-derived lead zirconate titanate (PZT) thin films due to the constrained shrinkage of the wet film during the drying, pyrolysis, densification, and crystallization processes. These residual stresses are further influenced by thermal expansion mismatch between the film and the substrate during cooling. In most cases, biaxial tensile residual stresses develop in PZT films deposited on platinized silicon substrates (Si/SiO₂/Ti/Pt), leading to an in-plane clamping effect that restricts domain motion⁵⁰. This clamping effect significantly reduces both in-plane and out-of-plane field-induced strains, thereby altering the effective piezoelectric response. The impact of residual stress is further complicated by its close relationship with film texture. Tuttle et al.²⁷ demonstrated that the stress state experienced by a PZT film during cooling through the Curie temperature (T_c) directly influences the preferred domain orientation. Tensile stresses during cooling promote an "a-domain" configuration, where the polarization vector aligns parallel to the substrate, whereas compressive stresses favor a "c-domain" configuration, where the polarization vector aligns perpendicular to the substrate. Consequently, PZT films with different textures may experience different residual stress states when deposited on stiff substrates, contributing to the variation in their linear and nonlinear ferroelectric properties^{28,50}. Another key factor affecting residual stress is film thickness. Thin PZT films experience higher residual stresses compared to thicker films, leading to lower effective piezoelectric coefficients^{12,50}. However, studies have shown that PZT films of different thicknesses but with similar residual stress values exhibit comparable piezoelectric responses¹². This finding suggests that residual stress, rather than film thickness, is the dominant factor governing the electromechanical response of PZT films.

Figure 8(a) illustrates the effect of equibiaxial tensile stress on the strain (e_{33}) vs. applied electric field (E_3) response for randomly oriented polycrystalline PZT. As tensile stress increases, the piezoelectric coefficient d_{33} —determined from the slope of the strain-electric field curve—decreases. This reduction in d_{33} is attributed to the increased in-plane clamping effect, which restricts domain motion and reduces out-of-plane displacement, leading to a lower strain response under the same applied electric field. Similarly, Figure 8(b) and (c) illustrate the decline in the piezoelectric coefficients (d_{33} and d_{31}) with increasing tensile residual stress across different textures. However, the rates of decrease vary depending on the texture, highlighting that the impact of residual stress is highly texture dependent.

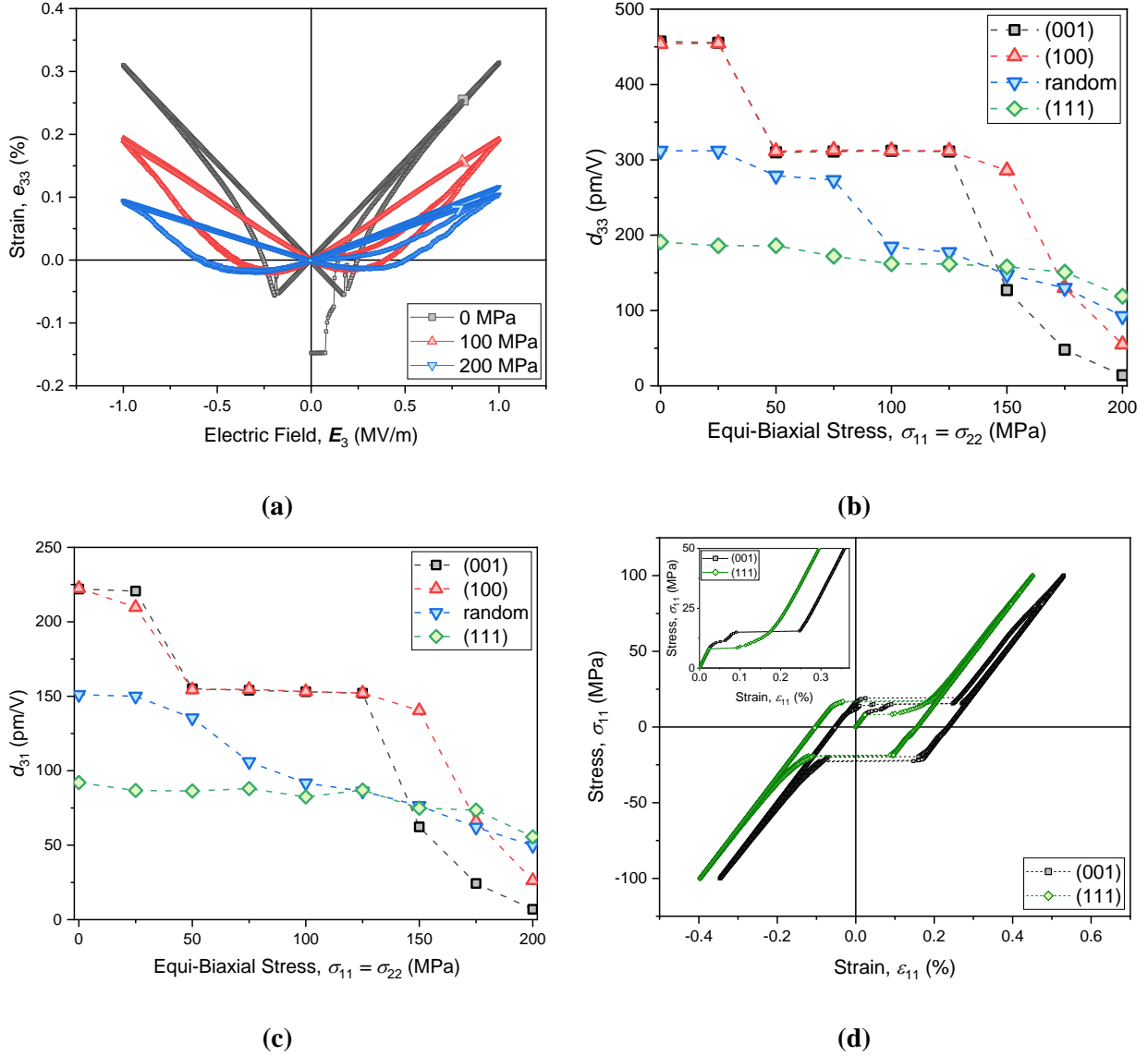


Figure 8. (a) Effect of equi-biaxial tensile stress on the strain (e_{33}) vs electric field (E_3) response of randomly oriented PZT. The slope, and hence the piezoelectric coefficient, decreases with increases in tensile stress. Decrease in piezoelectric coefficients (b) d_{33} , and (c) d_{31} with increase in equi-biaxial tension and for a standard deviation of $\pi/30$. The d_{33} and d_{31} drops the maximum for (001) texture whereas it is relatively stable (unchanging) for the (111) texture. (d) Stress (σ_{11}) vs strain (ϵ_{11}) response of (001) and (111) oriented PZT. The (001) texture shows more non-linear effects (inset) as compared to (111) texture which shows less domain-switching strains.

It is important to distinguish this observation from the previous discussion, where residual stress influenced the development of texture during film processing. In contrast, the focus here is on the electromechanical response of a material with a given texture, analyzing how residual stress

alters its piezoelectric behavior rather than its initial domain structure or crystallographic alignment. As shown in Figures 8(b) and 8(c), d_{33} values exhibit the greatest drop in (001)-textured crystallites, while they remain relatively stable for (111)-textured crystallites. This suggests that (001) texture, while producing the highest piezoelectric strain response in low-stress conditions, is significantly more susceptible to degradation under high residual stress. Conversely, (111) texture demonstrates greater robustness under elevated stress conditions, maintaining more consistent electromechanical properties. At sufficiently high residual stress levels (e.g., 200 MPa in Fig. 8(b) and 8(c)), the piezoelectric response of (111)-textured crystallites or even randomly oriented crystallites may surpass that of (001)-textured crystallites, a trend that has also been observed in experimental studies^{23,25}. Without accounting for residual stress, variations in piezoelectric response across different textures may be misattributed solely to crystallographic orientation, potentially leading to inaccurate comparisons and conclusions. These findings emphasize the critical importance of reporting residual stress values when comparing piezoelectric strain coefficients in PZT films. Understanding the impact of residual stress is essential for optimizing the design of PZT-based devices, particularly in applications where films are subjected to large mechanical constraints or thermal cycling.

Figure 8(d) presents the stress (σ_{11}) vs. strain (ϵ_{11}) response for (001)- and (111)-oriented PZT, illustrating the tension-unloading-compression-unloading cycle. While ceramics are typically designed to operate under compressive loading due to their inherent flaw sensitivity in tension, thin PZT films in d_{31} -flexural mode experience both tensile and compressive stresses. Therefore, the tension-compression response is analyzed to understand the electromechanical behavior of these films under practical operating conditions. The inset highlights a key distinction in ferroelastic behavior: (001)-textured PZT exhibits greater non-linearity, characterized by a larger strain jump during domain switching, whereas (111)-textured PZT shows reduced domain-switching strains and less deviation from the initial elastic path. This indicates that (001)-oriented crystallites undergo more pronounced ferroelastic switching, leading to greater hysteresis, whereas (111)-oriented crystallites exhibit a more stable and linear stress-strain response. The increased ferroelastic non-linearity in (001)-textured PZT compared to (111)-textured PZT has been previously reported in studies on MPB compositions⁹, further reinforcing the texture-dependent nature of ferroelastic switching in PZT.

Figure 9 illustrates the evolution of polarization vectors under the application of a maximum electric field (E_3) in ferroelectric ceramics with different crystallographic textures—(001), (100), and (111)—at the MPB composition for four different levels of equi-biaxial stress. The results highlight how increasing stress alters domain configurations and impacts the effective piezoelectric coefficients (d_{33} and d_{31}).

(001)-Textured Crystallites: In the absence of applied stress and electric field, the polarization vectors in (001)-textured crystallites exhibit a characteristic distribution reflecting the coexistence of tetragonal and rhombohedral domains. Tetragonal domains align along the top and bottom poles, whereas rhombohedral domains are distributed along two rings at a vertical angle of 54.7° from the poles, with some standard deviation. When a 25 MPa equi-biaxial stress is applied, tetragonal domains shift toward the equator, while rhombohedral domains remain near their original positions. Under the subsequent application of a maximum positive electric field, the tetragonal domains realign near the north pole, while rhombohedral domains cluster along the 54.7° ring in the northern hemisphere. However, as the in-plane stress increases to 50 MPa, the electric field is no longer sufficient to induce complete 90° domain switching in tetragonal crystallites. Instead, the polarization vectors form two distinct rings: one at the equator (tetragonal domains) and another at 54.7° (rhombohedral domains). This reduced domain switching results in a drop in d_{33} from 455 to 311 pC/N. For stress levels up to 125 MPa, the polarization configuration remains largely unchanged, and the slope of the butterfly loop continues to decrease gradually. However, at 150 MPa, the large in-plane stress induces a significant interphase domain switching, with a large fraction of rhombohedral domains transforming into tetragonal domains near the equator. As a result, d_{33} drops sharply from 311 to 127 pC/N, with 79% of domains becoming tetragonal under the applied maximum electric field. Beyond this point, the slope strictly decreases, and at 200 MPa, d_{33} is reduced to just 14 pC/N. Both d_{33} and d_{31} follow the same overall pattern, decreasing progressively with increasing stress (Fig. 8(b) and 8(c)).

(100)-Textured crystallites: The (100)-textured crystallites exhibit a response similar to (001)-textured crystallites under increasing equi-biaxial stress. However, beyond 150 MPa, the numerical values of d_{33} and d_{31} begin to diverge slightly between the two textures, despite following the same overall trend. This discrepancy arises because, even with the same standard deviation, the polarization vectors in (100)-textured crystallites are more widely dispersed compared to those in (001)-textured crystallites. The increased dispersion is attributed to

differences in angular constraint and distribution geometry. In (001)-textured crystallites, polarization vectors are clustered near the poles, resulting in a more localized spread. In contrast, (100)-textured crystallites distribute their polarization vectors along the equatorial plane, covering a broader angular region. Additionally, stereographic projection effects further amplify this apparent spread. This greater dispersion leads to a lower degree of interphase domain switching (rhombohedral \rightarrow tetragonal) under the same applied stress. As a result, at 150 MPa, only 55% of the domains in the (100) texture undergo tetragonal transformation and accumulate near the equator, compared to 79% in the (001) texture. This reduced transformation results in higher d_{33} and d_{31} values in (100)-textured crystallites relative to (001)-textured crystallites at equivalent stress levels.

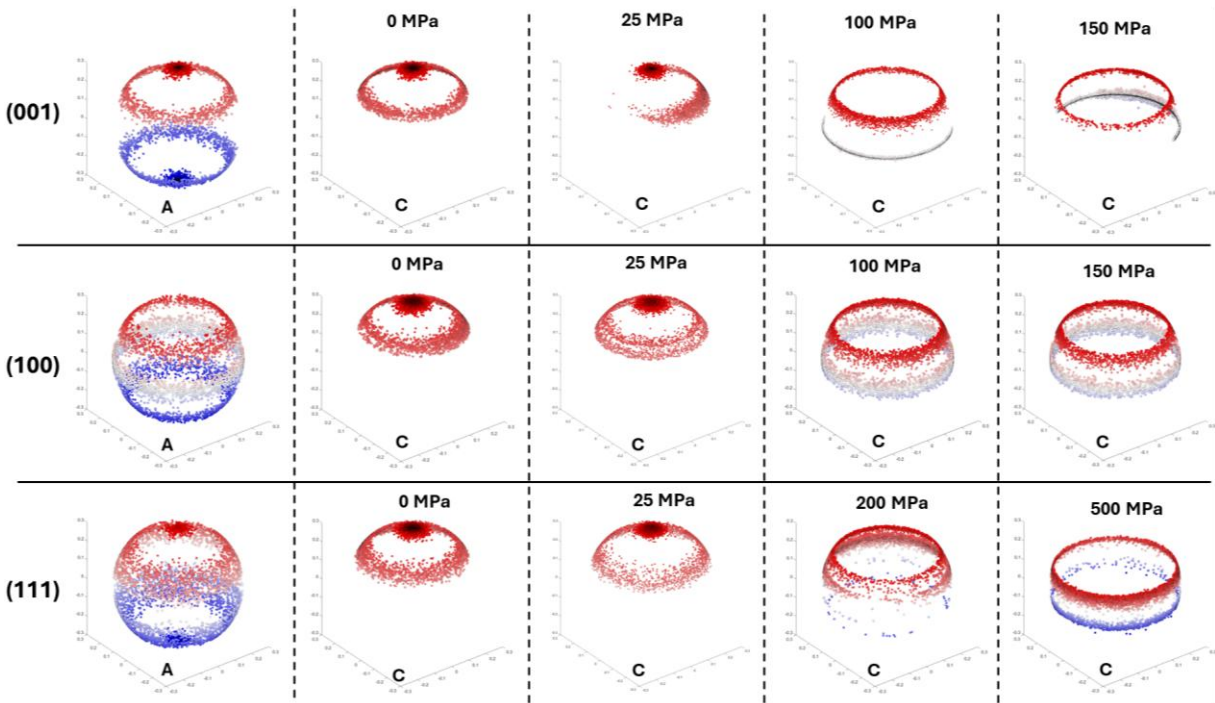


Figure 9. Polarization vectors in textured-MPB PZT at point A (initial configuration) and their evolution under applied in-plane equi-biaxial tension. Snapshots are shown for point C (1 MV/m positive electric field) at progressively increasing tensile stress levels. The vectors are constructed for a standard deviation of $\pi/30$.

(111)-Textured crystallites: In the initial unstressed state, the polarization vectors in (111)-textured crystallites are distributed around the top and bottom poles and two distinct circles in each hemisphere, with a standard deviation reflecting polycrystalline misorientation. Tetragonal domains cluster along a 54.7° vertical ring from the poles. Rhombohedral domains align along the

poles and a second ring at 71° from the poles. Upon applying an electric field, the polarization vectors from the lower hemisphere shift to the upper hemisphere (see Fig. 7). However, due to the absence of domains near the equator, even at high in-plane stress levels (up to 175 MPa), there is minimal change in the butterfly loop slope. Unlike (001) and (100) textures, (111)-textured crystallites experience less interphase domain switching, and the overall piezoelectric response remains relatively stable. The primary effect of stress is a minor rearrangement of domain orientations, leading to only a slight reduction in d_{33} and d_{31} rather than a significant degradation. At 200 MPa, a small but noticeable decrease in both d_{33} and d_{31} occurs, primarily due to interphase domain switching from tetragonal to rhombohedral domains. Since rhombohedral domains are closer to the equator in (111)-textured crystallites, the stress-driven transformation follows an opposite trend compared to (001) and (100) textures. However, if stress levels reach 500 MPa, even under a maximum electric field, two distinct polarization rings form in the northern and southern hemispheres, effectively neutralizing the piezoelectric response and reducing butterfly loop slopes to near zero.

Randomly Oriented crystallites: For randomly oriented crystallites, the response exhibits a continuous decrease in piezoelectric coefficients with increasing stress. Unlike the more distinct transitions observed in highly textured samples, interphase domain switching begins gradually between 125 MPa and 150 MPa, leading to a progressive degradation of piezoelectric performance.

The interplay between equibiaxial stress, texture, and domain switching mechanisms significantly impacts the electromechanical response of PZT at MPB. While (001)- and (100)-textured crystallites exhibit superior piezoelectric performance in low-stress conditions, their response degrades significantly beyond 150 MPa due to extensive stress-induced domain transformations. In contrast, (111)-textured crystallites maintain a more stable electromechanical response due to their reduced susceptibility to stress-induced domain switching. These findings emphasize the importance of considering residual stress effects when evaluating piezoelectric performance, particularly in thin-film applications where large in-plane stresses are prevalent.

4.6. *Fitting Experimental Data*

In this final section, we demonstrate that the model can effectively fit experimental data for both randomly oriented and textured PZT. Figure 10 presents the comparison between numerical simulations and experimental measurements, with the parameters used for fitting are provided in Table 3.

For randomly oriented PZT at the MPB composition, Fig. 10(a) shows that the model successfully captures the e_{33} vs. E_3 butterfly loop from the experimental work of Saito *et al.*⁵¹. However, at high electric fields, the experimental data deviates from the numerical prediction, especially on the side of the positive electric field. This discrepancy arises because the model, like most existing models, does not fully account for the reduction in extrinsic contributions—particularly domain wall motion saturation—which leads to an overestimation of strain in the high-field regime.

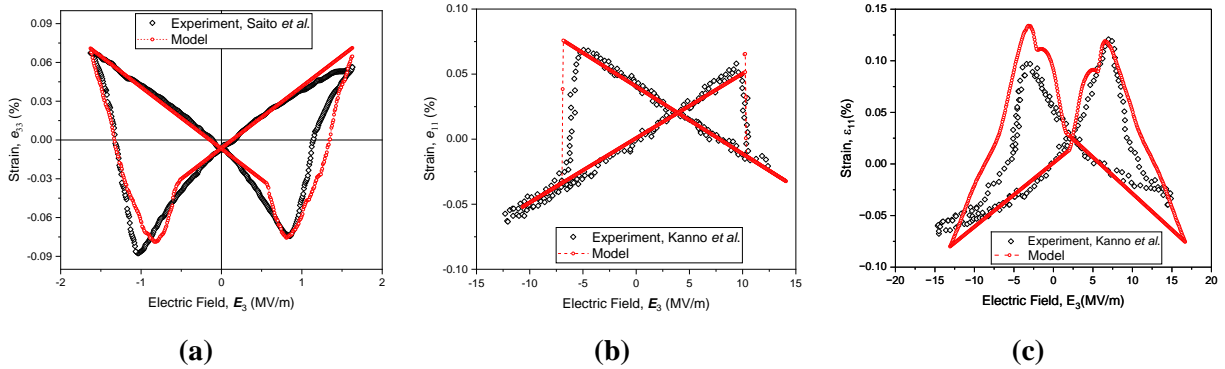


Figure 10. Comparison between experimental data and computational model predictions for: (a) randomly oriented MPB PZT⁵¹, (b) (001)-textured PZT thin film⁴⁵, and (c) dominantly (111)-textured PZT thin film⁴⁵. To facilitate direct comparison, the model curves have been translated and shifted to align with the experimental intersection points while preserving the relative trends in electromechanical response.

To validate the model for textured PZT, we referenced experimental cantilever deflection data from the work of Kanno *et al.*⁴⁵, due to the limited availability of textured bulk PZT data in the literature. The authors fabricated d_{31} -type PZT thin films (2.9 μm and 2.5 μm thick) on two different substrates: (100)Pt/(100)MgO, which resulted in a predominantly (001)-textured PZT, and (111)Pt/Ti/Si, which produced a predominantly (111)-textured PZT. Cantilever tip deflection was measured using a bipolar sine wave signal ($\pm 35\text{V}$, 10 Hz), and the recorded deflection vs. voltage data was converted to strain (e_{11}) vs. electric field (E_3) using the multimorph deflection model by DeVoe *et al.*⁵². This model requires input parameters such as flexural rigidities and layer

thicknesses, which allow for the calculation of d_{31} as a function of E_3 . The strain reported here is the e_{11} strain, which is the product of d_{31} and E_3 . The film in-plane Young's modulus of Pt was taken from the work of Das *et al.*⁵³, while the thin Au layer was assumed to have a modulus of 40 GPa.

Table 3: Parameters used for fitting experimental data

Parameter	Saito <i>et al.</i> ⁵¹	Kanno <i>et al.</i> [001] ⁴⁵	Kanno <i>et al.</i> [111] ⁴⁵
\bar{E}_0^{90} (MV/m)	0.7	4.2	2
\bar{E}_0^{180} (MV/m)	2	12	12
\bar{E}_0^{71-109} (MV/m)	0.7	5	4
\bar{E}_0^{55-125} (MV/m)	1.5	10	10
d_{ijk}	$d_{ijk}/5$ (tetragonal)	$d_{ijk}/40$ (tetragonal)	$d_{ijk}/25$ (tetragonal)
N	500	2000	5000
e_{33} shift	0.05%	-	-
e_{11} shift	-	0.02%	0
E_3 shift (MV/m)	-	Flipped and 1.8	Flipped and 1.7
Standard Deviation (rad)	N/A (random texture)	0	$\pi/10$
Biaxial Stress (MPa)	45	0	200 (uniaxial)

Figure 10(b) shows the e_{11} strain response for the cantilever with a c-axis oriented PZT film on MgO. The experimental strain vs field curve exhibits an ideal butterfly loop with distinct 180° domain switching. Apart from the 180° switching, the strain in the PZT layer shows excellent linearity, attributed to the highly oriented c-axis texture of the PZT film. The model successfully captures both domain switching behavior and the linearity of the response. In contrast, the strain-field response for the PZT film on a Si substrate exhibits significant displacement hysteresis, as shown in Fig. 10(c). This behavior arises because, in addition to intrinsic lattice motion, the piezoelectric strain is also influenced by off-axis domain reorientation, particularly 90° domain switching. The theoretical model effectively captures this effect, demonstrating its capability to account for both lattice-driven and domain-driven strain contributions.

The numerical model, thus, successfully reproduces experimental butterfly loops for both randomly oriented and textured PZT. The ability of the model to capture domain switching

mechanisms and texture-dependent strain behavior makes it a valuable tool for understanding and optimizing electromechanical responses in PZT-based devices.

5. Conclusion

This computational study elucidated the influence of texture and applied stress on the electromechanical response of PZT at the MPB composition. The results confirm that the piezoelectric response is maximized at the MPB, where texture plays a critical role in governing polarization orientation and domain switching behavior. Notably, (001)-textured material exhibits the highest piezoelectric coefficients at low stress or residual stress conditions, even with a standard deviation of approximately 25° in crystallite orientation, which reflects the degree of alignment. Additionally, the study highlights the distinction between (001)- and (100)-textured material when considering variability in crystallite orientation. The ratio $d_{31(001)}/d_{31(111)}$ reaches a theoretical maximum of ~ 2.6 , and experimental data with near-perfect texturing show that it approaches ~ 2.5 . Other experiments show a value in the range of 1.5 – 2.1. This highlights the necessity of characterizing not only the dominant texture but also the distribution of crystallite orientations when evaluating ferroelectric ceramics. The study further reveals that stress-induced modifications in domain switching dynamics are pivotal in shaping the electromechanical response. While (001)- and (100)-textured crystallites demonstrate superior piezoelectric performance in low-stress conditions, their response degrades beyond 150 MPa due to extensive domain transformations. In contrast, (111)-textured crystallites (or even randomly oriented crystallites) exhibit a more stable electromechanical response. Additionally, the uniaxial stress-strain response of (111)-textured material is more linear than that of (001)-textured material, consistent with experimental observations. These findings emphasize the critical role of residual stress in piezoelectric performance, particularly in thin-film applications, where large in-plane stresses can significantly impact material behavior. By providing deeper insight into the interplay between crystallographic texture, stress state, and ferroelectric domain behavior, this study offers valuable guidance for optimizing piezoelectric performance in PZT-based devices.

6. Acknowledgement

The authors acknowledge support from the Indian Institute of Science through seed grants (IE/CARE-21-0355) and (IE/RERE-21-0610).

7. Data and Code Availability

Code can be found in the **supplementary material** section.

8. Conflict of Interest Statement

The authors declare no competing financial or non-financial interests.

9. References

¹ H. Kim, S. Priya, H. Stephanou, and K. Uchino, “Consideration of Impedance Matching Techniques for Efficient Piezoelectric Energy Harvesting,” *IEEE Trans. Ultrason. Ferroelectr. Freq. Control* **54**(9), 1851–1859 (2007).

² G.L. Smith, J.S. Pulskamp, L.M. Sanchez, D.M. Potrepka, R.M. Proie, T.G. Ivanov, R.Q. Rudy, W.D. Nothwang, S.S. Bedair, C.D. Meyer, and R.G. Polcawich, “PZT -Based Piezoelectric MEMS Technology,” *J. Am. Ceram. Soc.* **95**(6), 1777–1792 (2012).

³ M. Murata, T. Kondoh, T. Yagi, N. Funatsu, K. Tanaka, H. Tsukuni, K. Ohno, H. Usami, R. Nayve, N. Inoue, S. Seto, and N. Morita, “High-Resolution Piezo Inkjet Printhead Fabricated by Three Dimensional Electrical Connection Method using through Glass VIA,” in *2009 IEEE 22nd Int. Conf. Micro Electro Mech. Syst.*, (IEEE, 2009), pp. 507–510.

⁴ P. Muralt, “Piezoelectric Films for Innovations in the Field of MEMS and Biosensors,” in *Piezoelectricity*, (Springer Berlin Heidelberg, Berlin, Heidelberg, 2008), pp. 351–376.

⁵ J.R. Bronson, J.S. Pulskamp, R.G. Polcawich, C.M. Kroninger, and E.D. Wetzel, “PZT MEMS Actuated Flapping Wings for Insect-Inspired Robotics,” in *2009 IEEE 22nd Int. Conf. Micro Electro Mech. Syst.*, (IEEE, 2009), pp. 1047–1050.

⁶ J.S. Pulskamp, R.G. Polcawich, R.Q. Rudy, S.S. Bedair, R.M. Proie, T. Ivanov, and G.L. Smith, “Piezoelectric PZT MEMS technologies for small-scale robotics and RF applications,” *MRS Bull.* **37**(11), 1062–1070 (2012).

⁷ B. Jaffe, W.R. Cook, and H. Jaffe, *Piezoelectric Ceramics* (Academic Press London, 1971).

⁸ J. Li, W. Qu, J. Daniels, H. Wu, L. Liu, J. Wu, M. Wang, S. Checchia, S. Yang, H. Lei, R. Lv, Y. Zhang, D. Wang, X. Li, X. Ding, J. Sun, Z. Xu, Y. Chang, S. Zhang, and F. Li, “Lead zirconate titanate ceramics with aligned crystallite grains,” *Science* (80-.). **380**(6640), 87–93 (2023).

⁹ D. Das, L. Sanchez, J. Martin, B. Power, S. Isaacson, R.G. Polcawich, and I. Chasiotis, “Control of mechanical response of freestanding PbZr_{0.52}Ti_{0.48}O₃ films through texture,” *Appl. Phys. Lett.* **109**(13), 131905 (2016).

¹⁰ D. Das, L. Sanchez, J. Martin, B. Power, S. Isaacson, R.G. Polcawich, and I. Chasiotis, “Control of ferroelectric and linear piezoelectric response of PZT films through texture,” *J. Am. Ceram. Soc.* **101**(7), 2965–2975 (2018).

¹¹ L. Lian, and N.R. Sottos, “Stress effects in sol-gel derived ferroelectric thin films,” *J. Appl. Phys.* **95**(2), 629 (2004).

¹² T.A. Berfield, R.J. Ong, D.A. Payne, and N.R. Sottos, “Residual stress effects on piezoelectric response of sol-gel derived lead zirconate titanate thin films,” *J. Appl. Phys.* **101**(2), 024102 (2007).

¹³ T. Lee, H. Lee, S. Park, T. Lee, D. Kim, C. Hong, H. Xu, C. Kang, and S. Nahm, “Structural and piezoelectric properties of <001> textured PZT - PZNN piezoelectric ceramics,” *J. Am. Ceram. Soc.* **100**(12), 5681–5692 (2017).

¹⁴ N. Ledermann, P. Muralt, J. Baborowski, S. Gentil, K. Mukati, M. Cantoni, A. Seifert, and N. Setter, “{1 0 0}-Textured, piezoelectric Pb(Zrx, Ti_{1-x})O₃ thin films for MEMS: integration, deposition and properties,” *Sensors Actuators A Phys.* **105**(2), 162–170 (2003).

¹⁵ X. Du, J. Zheng, U. Belegundu, and K. Uchino, “Crystal orientation dependence of piezoelectric properties of lead zirconate titanate near the morphotropic phase boundary,” *Appl. Phys. Lett.* **72**(19), 2421 (1998).

¹⁶ J. Wu, S. Zhang, and F. Li, “Prospect of texture engineered ferroelectric ceramics,” *Appl. Phys. Lett.* **121**(12), (2022).

¹⁷ N. Shen, Q. Liao, Y. Liao, R. Li, Y. Zhang, S. Song, Y. Song, C. Zhu, and L. Qin, “Development Status of Textured Piezoelectric Ceramics and Preparation Processes,” *Coatings* **15**(1), 51 (2025).

¹⁸ Y. Yan, L.D. Geng, L. Zhu, H. Leng, X. Li, H. Liu, D. Lin, K. Wang, Y.U. Wang, and S. Priya, “Ultrahigh Piezoelectric Performance through Synergistic Compositional and Microstructural Engineering,” *Adv. Sci.* **9**(14), 1–10 (2022).

¹⁹ L.M. Sanchez, D.M. Potrepka, G.R. Fox, I. Takeuchi, K. Wang, L. a. Bendersky, and R.G. Polcawich, “Optimization of PbTiO₃ seed layers and Pt metallization for PZT-based piezoMEMS actuators,” *J. Mater. Res.* **28**(14), 1920–1931 (2013).

²⁰ N. Izyumskaya, Y.I. Alivov, S.J. Cho, H. Morkoç, H. Lee, and Y.S. Kang, “Processing, structure, properties, and applications of PZT thin films,” *Crit. Rev. Solid State Mater. Sci.* **32**(3–4), 111–202 (2007).

²¹ H.G. Yeo, and S. Trolier-McKinstry, “{001} Oriented piezoelectric films prepared by chemical solution deposition on Ni foils,” *J. Appl. Phys.* **116**(1), 014105 (2014).

²² X.X.-H. Du, J. Zheng, U. Belegundu, and K. Uchino, “Crystal orientation dependence of piezoelectric properties of lead zirconate titanate near the morphotropic phase boundary,” *Appl. Phys. Lett.* **72**(19), 2421 (1998).

²³ F. Xu, R.A. Wolf, T. Yoshimura, and S. Trolier-McKinstry, “Piezoelectric films for MEMS applications,” in *Proceedings. 11th Int. Symp. Electrets*, (IEEE, 2002), pp. 386–396.

²⁴ D. Ambika, V. Kumar, K. Tomioka, and I. Kanno, “Deposition of PZT thin films with (001), (110), and (111) crystallographic orientations and their transverse piezoelectric characteristics,” *Adv. Mater. Lett.* **3**(2), 102–106 (2012).

²⁵ K. Kakimoto, H. Kakimoto, S. Fujita, and Y. Masuda, “Control of Crystal Orientation and Piezoelectric Response of Lead Zirconate Titanate Thin Films Near the Morphotropic Phase Boundary,” *J. Am. Ceram. Soc.* **85**(4), 1019–1021 (2004).

²⁶ R.J. Ong, T. a. Berfield, N.R. Sottos, and D. a. Payne, “Sol-Gel derived Pb(Zr,Ti)O₃ thin films: Residual stress and electrical properties,” *J. Eur. Ceram. Soc.* **25**(12 SPEC. ISS.), 2247–2251 (2005).

²⁷ B.A. Tuttle, J.A. Voigt, T.J. Garino, D.C. Goodnow, R.W. Schwartz, D.L. Lamppa, T.J. Headley, and M.O. Eatough, “Chemically prepared Pb(Zr,Ti)O₃ thin films: the effects of orientation and stress,” in *ISAF '92 Proc. Eighth IEEE Int. Symp. Appl. Ferroelectr.*, (IEEE, 1992), pp. 344–348.

²⁸ S. Trolier-McKinstry, and P. Muralt, “Thin Film Piezoelectrics for MEMS,” *J. Electroceramics* **12**(1), 7–17 (2004).

²⁹ S.C. Hwang, J.E. Huber, R.M. McMeeking, and N.A. Fleck, “The simulation of switching in polycrystalline ferroelectric ceramics,” *J. Appl. Phys.* **84**(3), 1530–1540 (1998).

³⁰ J. Huber, “A constitutive model for ferroelectric polycrystals,” *J. Mech. Phys. Solids* **47**(8), 1663–1697 (1999).

³¹ F.X. Li, and R.K.N.D. Rajapakse, “A constrained domain-switching model for polycrystalline ferroelectric ceramics. Part I: Model formulation and application to tetragonal materials,” *Acta Mater.* **55**(19), 6472–6480 (2007).

³² F.X. Li, and R.K.N.D. Rajapakse, “A constrained domain-switching model for polycrystalline ferroelectric ceramics. Part II: Combined switching and application to rhombohedral materials,” *Acta Mater.* **55**(19), 6481–6488 (2007).

³³ J.Y. Li, R.C. Rogan, E. Ustündag, and K. Bhattacharya, “Domain switching in polycrystalline ferroelectric ceramics,” *Nat. Mater.* **4**(10), 776–781 (2005).

³⁴ F.X. Li, and Y.W. Li, “Modeling on domain switching in ferroelectric ceramics near the morphotropic phase boundary,” *J. Appl. Phys.* **105**(12), (2009).

³⁵ Y.W. Li, X.L. Zhou, H.C. Miao, H.R. Cai, and F.X. Li, “Mechanism of crystal-symmetry dependent deformation in ferroelectric ceramics: Experiments versus model,” *J. Appl. Phys.* **113**(21), (2013).

³⁶ J.E. Huber, and N.A. Fleck, “Multi-axial electrical switching of a ferroelectric: theory versus experiment,” *J. Mech. Phys. Solids* **49**(4), 785–811 (2001).

³⁷ R.E. García, B.D. Huey, and J.E. Blendell, “Virtual piezoforce microscopy of polycrystalline ferroelectric films,” *J. Appl. Phys.* **100**(6), 0–10 (2006).

³⁸ H.A. Murdoch, and R.E. Garcia, “Crystallographic texture optimisation in

polycrystalline ferroelectric films for Random Access Memory applications,” *Int. J. Mater. Prod. Technol.* **35**(3/4), 293 (2009).

³⁹ S.C. Hwang, J.E. Huber, R.M. McMeeking, and N.A. Fleck, “The prediction of switching in polycrystalline ferroelectric ceramics,” *J. Appl. Phys.* **84**(3), 1530–1540 (1998).

⁴⁰ M.J. Haun, E. Furman, S.J. Jang, and L.E. Cross, “Thermodynamic theory of the lead zirconate-titanate solid solution system, part V: Theoretical calculations,” *Ferroelectrics* **99**(1), 63–86 (1989).

⁴¹ J. Holland, “Angles,” (<https://www.geogebra.org/m/HfqAet9S>).

⁴² X. Du, U. Belegundu, and K. Uchino, “Crystal Orientation Dependence of Piezoelectric Properties in Lead Zirconate Titanate: Theoretical Expectation for Thin Films,” *Jpn. J. Appl. Phys.* **36**(Part 1, No. 9A), 5580–5587 (1997).

⁴³ D. a. Berlincourt, C. Cmolik, and H. Jaffe, “Piezoelectric Properties of Polycrystalline Lead Titanate Zirconate Compositions,” *Proc. IRE* **48**(2), 220–229 (1960).

⁴⁴ M. Cuffe, M. Allain, J. Abergel, G. Le Rhun, M. Aid, E. Defay, and D. Faralli, “Influence of the crystallographic orientation of $\text{Pb}(\text{Zr},\text{Ti})\text{O}_3$ films on the transverse piezoelectric coefficient d_{31} ,” in *2011 IEEE Int. Ultrason. Symp.*, (IEEE, 2011), pp. 1948–1951.

⁴⁵ I. Kanno, H. Kotera, and K. Wasa, “Measurement of transverse piezoelectric properties of PZT thin films,” *Sensors Actuators A Phys.* **107**(1), 68–74 (2003).

⁴⁶ C. Ayela, L. Nicu, C. Soyer, E. Cattan, and C. Bergaud, “Determination of the d_{31} piezoelectric coefficient of $\text{PbZr}_x\text{Ti}_{1-x}\text{O}_3$ thin films using multilayer buckled micromembranes,” *J. Appl. Phys.* **100**(5), 054908 (2006).

⁴⁷ J. Akedo, and M. Lebedev, “Piezoelectric properties and poling effect of $\text{Pb}(\text{Zr}, \text{Ti})\text{O}_3$ thick films prepared for microactuators by aerosol deposition,” *Appl. Phys. Lett.* **77**(11), 1710–1712 (2000).

⁴⁸ D. Das, *Electromechanical Response of Textured Ferroelectric PZT Thin Film Stacks*, University of Illinois at Urbana-Champaign, 2017.

⁴⁹ H. Leng, Y. Yan, X. Li, S.K. Karan, M. Fanton, and S. Priya, “High-power piezoelectric behavior of acceptor-doped $\langle 001 \rangle$ and $\langle 111 \rangle$ textured piezoelectric ceramics,” *J. Mater.*

Chem. C **11**(6), 2229–2240 (2023).

⁵⁰ L. Lian, and N.R. Sottos, “Effects of thickness on the piezoelectric and dielectric properties of lead zirconate titanate thin films,” *J. Appl. Phys.* **87**(8), 3941 (2000).

⁵¹ Y. Saito, and S. Hori, “Acoustic emission and domain switching in tetragonal lead zirconate titanate ceramics,” *Jpn. J. Appl. Phys.* **33**(9 S), 5555–5558 (1994).

⁵² D.L. DeVoe, and A.P. Pisano, “Modeling and optimal design of piezoelectric cantilever microactuators,” *J. Microelectromechanical Syst.* **6**(3), 266–270 (1997).

⁵³ D. Das, B. Power, J.P. Martin, R.G. Polcawich, and I. Chasiotis, “Role of oxide seed layer in plastic response of epitaxially grown textured metal films,” *Acta Mater.* **112**, 390–402 (2016).